

Flight-Ready Precise and Robust Carrier-Phase GNSS Navigation Software for Distributed Space Systems

Samuel Y. W. Low, Toby Bell and Simone D'Amico

Stanford University, Department of Aeronautics and Astronautics, Space Rendezvous Laboratory

ABSTRACT

This paper presents the full requirements analysis, design, development, and testing of high-precision navigation flight software for Distributed Space Systems (DSS) using Carrier Phase Differential GNSS (CDGNSS). Five main contributions are made. First, a survey of flown and upcoming DSS missions with stringent precision requirements is conducted, from which a thorough requirements analysis is distilled to guide development and testing. Second, a real-time navigation functional architecture is designed, and adopts a sparse and regularized Consider Kalman Filter with options for numerical stability in-flight. The filter rigorously accounts for uncertainties in process noise, measurement noise, and biases. It tracks float ambiguities with integer resolution where possible. The covariance correlation structure is preserved under all navigation modes, including contingencies and outages. Third, a lightweight, memoryless Fault Detection, Isolation, and Recovery (FDIR) module is developed to guard against anomalous measurements, providing statistical screening and ensuring robust navigation. Fourth, the software architecture is proposed for ease of integration, with strategies presented for modularity and computational efficiency tailored to constrained flight systems. Fifth, a comprehensive test campaign is conducted, mapped to a requirements verification matrix, spanning unit, interface, software-in-the-loop, and real-time hardware-in-the-loop tests, emphasizing gradual test fidelity for efficient fault isolation. Finally, flight-like results are demonstrated using the VISORS mission, due to the generalizability of the VISORS navigation operations, and the stringency which demands sub-centimeter relative position and sub-millimeter-per-second velocity accuracy. This architecture aims to serve as a reference for next-generation DSS missions adopting CDGNSS.

TABLE OF ABBREVIATIONS

CDGNSS	Carrier Phase Differential GNSS	CEKF	Consider Extended Kalman Filter	COM	Center of Mass
DDCP	Double Difference Carrier Phase	DSS	Distributed Space Systems	ECI	Earth-Centered Inertial Frame
EKF	Extended Kalman Filter	EOP	Earth Orientation Parameters	FDIR	Fault Detection, Isolation and Recovery
GRAPHIC	Group and Phase Ionospheric Calibration	IAR	Integer Ambiguity Resolution	PCO	Phase Center Offset
PCV	Phase Center Variations	RTN	Radial-Tangential-Normal Frame	SDCP	Single Difference Carrier Phase
STM	State Transition Matrix	UKF	Unscented Kalman Filter	ZDCP	Zero Difference Carrier Phase

I. INTRODUCTION

Precise relative navigation is a key enabler for emerging Distributed Space Systems (DSS), unlocking science not possible with monolithic spacecraft [1]. Distributed apertures, for instance, enable multi-static sensing, virtual telescoping, radio localization, gravimetry, and interferometry. Carrier Phase Differential GNSS (CDGNSS), often with Integer Ambiguity Resolution (IAR) [2], have seen increasing onboard adoption. Earlier missions like GRACE [3] and TanDEM-X [4] used post-processed batch CDGNSS with IAR on the ground. Recent advances support real-time onboard execution to meet stricter requirements [5]. PRISMA (2010) [6] demonstrated real-time onboard CDGNSS with Single Difference Carrier Phase (SDCP) float ambiguity estimation, achieving $\leq 5\text{cm}$ and 1mm/s baseline errors. Can-X 4/5 (2014) [7, 8] achieved $\leq 10\text{cm}$ in a CubeSat using an automotive-grade NovAtel OEMV-1G receiver. These missions serve as pathfinders for low-cost, high-impact science using CDGNSS. In future, the VISORS virtual telescope will employ L1-only CDGNSS with IAR for mm-level alignment across 40m baselines [9, 10], using a NovAtel OEM7 and laser rangefinder, for solar imaging. The mDOT star shade mission applies CDGNSS with differential ionospheric correction across 500km, for host starlight suppression and exoplanet detection [11, 12, 13]. Future pathfinders for spaceborne laser interferometry, like STARI [14] and SILVIA [15], propose to fuse CDGNSS with optical metrologies for micro-arcsecond imaging of exoplanets and black hole accretion disks. These missions, summarized in Table 1, serve as the foundation of our requirements analysis.

The maturation of CDGNSS-based navigation parallels the growing availability and flight heritage of commercial-grade GNSS receivers, as seen in Can-X 4/5 [8] and VISORS [10]. CDGNSS has been studied for DSS for over two decades [16, 17], but adoption was initially hindered by costs and compute constraints. Today, new high-precision DSS mission concepts leveraging CDGNSS continue to be proposed [14, 15, 18, 19], while CDGNSS navigation architectures see ongoing advancement. One example is the *Distributed Multi-GNSS Timing and Localization* (DiGiTaL) flight software, which builds on PRISMA [6] and processes multi-GNSS measurements using a hybrid EKF-UKF architecture. DiGiTaL includes computational optimizations to

the UKF that enable measurement updates every 30s with real-time onboard IAR—never before demonstrated in-flight [20, 21]. Sensor fusion with DiGiTaL has been explored using vision-based angles-only measurements at far-range and image-based pose estimation at close-range [22]. Tight coupling of angles-only and range measurements within the integer search process has demonstrated improved IAR accuracy in noisy environments, potentially enabling IAR in HEO/GEO sidelobe-only scenarios [23]. For the N -spacecraft case, scalability of the software has been explored briefly [21], and search-based optimization of attitude pointing profiles have been proposed to support such navigation ops in larger swarms [24].

Table 1: Survey of contemporary distributed space missions exploiting GNSS for precision applications

Year	Mission	Mass [kg]	Purpose	Orbit & Altitude	Operation Baseline	Methodology	Baseline Accuracy
2002	GRACE [3]	487×2	Gravimetric Modeling	Polar LEO, 500km	170 to 270km	Ground post-processed CDGNSS with IAR, with K-Band range aiding	$\leq 1\text{mm}$
2010	TanDEM-X [4]	1230 & 1330	InSAR & Elevation Mapping	Polar LEO, 514km	250 to 500m	Ground post-processed CDGNSS with IAR, with ground satellite laser ranging	$\sim \text{cm}$
2010	PRISMA [6, 25]	150 & 40	Formation Flying Demo	LEO, 700km	100m to 2km	Real-time onboard CDGNSS float ambiguity estimation	$\leq 10\text{cm}$
2014	Can-X 4/5 [7, 8]	6.5×2	Formation Flying Demo	Polar LEO, 650km	50m to 1km	Real-time onboard CDGNSS float ambiguity estimation	$\leq 10\text{cm}$
2018	GRACE-FO [26, 27]	600×2	Gravimetric Modeling	Polar LEO, 490km	220km	Ground post-processed CDGNSS with IAR, with onboard laser interferometry	$\leq 1\text{mm}$
2022	CPOD [28, 29]	4.5×2	RPOD Tech Demo	LEO, $\sim 500\text{km}$	361m to 997km	Real-time onboard fusion of GPS pseudorange with crosslink range and camera measurements	$\sim \text{meters}$
2024	PROBA-3 [30, 31, 32]	340 & 200	Distributed Telescopy	HEO, 600 to 60,530km	200m to 2km	Ground post-processed GNSS at perigee; laser ranging, vision and shadow position sensors at apogee	$\sim \text{mm}$
~ 2026	VISORS [9, 10]	10 & 11	Distributed Telescopy	Polar LEO, 500 - 600km	40 to 200m	Real-time onboard CDGNSS with IAR, with laser ranging during observations	$\sim \text{mm}$
Proposed	mDOT [11, 12, 13]	246 total	Exoplanet Detection	LEO, $\sim 500\text{km}$	500km	Real-time onboard CDGNSS with IAR	$\sim \text{mm}$
Proposed	STARI [14]	10×2	Interferometry Demo	LEO, $\sim 500\text{km}$	10 to 100m	Real-time onboard CDGNSS with IAR, possibly aided by LED-based image alignment measurements	$\sim \text{mm}$
Proposed	SILVIA [15]	100×3	Interferometry Demo	LEO, 500 - 600km	$\sim 100\text{m}$	Float-only CDGNSS (precise mode), laser and beam position sensors (ultra-precise)	$\sim \text{mm} - \mu\text{m}$

Despite advances in CDGNSS-based navigation, challenges remain. Emerging missions such as VISORS [9, 10], mDOT [12, 13], and STARI [14] impose increasingly stringent requirements but have yet to achieve the necessary navigation accuracy and robustness [33]. A key gap in the literature is the lack of an end-to-end architecture that: (i) addresses emerging requirements that are generalizable to emerging DSS missions, (ii) rigorously addresses state, measurement, and dynamic uncertainties, including during off-nominal scenarios, (iii) ensures robustness to realistic navigation errors and software faults, (iv) employs computationally efficient strategies for flight, and (v) implements a comprehensive test plan to close the requirements loop.

This paper addresses these gaps through the formal design and development of a DiGiTaL v2 flight software. [Section I](#) surveys relevant missions to ground a generalizable requirements analysis. [Section II](#) distills requirements into Interfacing, Functional, and Performance, covering all navigation modes including open-loop orbit prediction and both single and relative spacecraft navigation. [Section III](#) introduces a filter design that rigorously treats state, dynamics, and measurement uncertainty while preserving covariance correlations. It incorporates body-frame uncertainties via Consider Analyses, and proposes a novel Joseph-like Consider Kalman Filter not previously presented. [Section IV](#) couples the filter with a lightweight, memoryless FDIR module that leverages statistical guarantees to handle anomalous or faulty data. [Section V](#) details a modular software architecture for ease of software integration, the full execution logic, and compute optimizations to meet runtime requirements. [Section VI](#) describes a structured, requirements-driven test campaign, spanning unit tests to full-scale real-time hardware-in-the-loop tests, using VISORS as a case study. The VISORS campaign is readily generalizable to future DSS missions and serves as a strong benchmark for flight software evaluation. State-of-the-art modeling for the dynamics, measurements, subsystem packet latencies, subsystem errors, and body-frame uncertainties are included. Overall, this work provides a complete closed-loop process which is traceable from requirements, to algorithms and compliance tests, so as to advance the readiness of CDGNSS-based navigation software for next-generation DSS missions.

II. NAVIGATION REQUIREMENTS

II.1. Requirements Generalizations and Assumptions

This section presents a generalized set of CDGNSS-based navigation requirements catered to a set of generalized operating modes applicable to missions surveyed. Clearly defined requirements are essential for guiding design decisions, ensuring validation, and avoiding costly issues later in development lifecycle [34]. The first necessary assumption made is that the spacecraft in question are cooperative, communicable, and operating under main-lobe GNSS reception. For guidance, a general DSS mission may adopt the following modes in Figure 1,

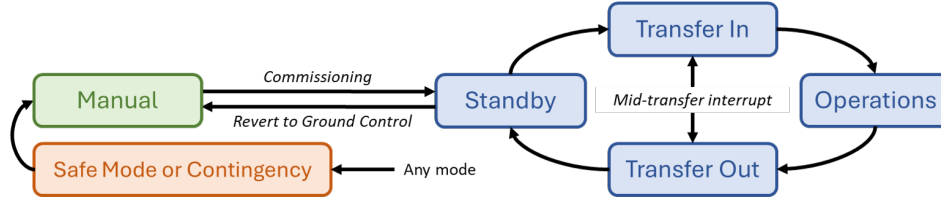


Figure 1: Generalized *modes* that spacecraft in a distributed system may adopt.

A *mode* is a logical abstraction of a spacecraft's current state meant to fulfil objectives or situational needs at each phase of the mission. With regards to software, different modes can adopt different configuration parameters and tailor compute resources to each phase of the mission. With regards to ops, different modes are often also characterized by different operating baselines, relative orbital elements, and passive safety margins [35]. The purpose of the abstraction in Figure 1 is to provide a context in which we present requirements, and cater them in accordance to the generalized stringency of each mode. Broadly, Standby mode is purposed for subsystem health monitoring and software checkouts prior to Transfer, which is a relative orbit reconfiguration trajectory, into Operations, which is purposed for execution of science or the payload. Generally, navigation accuracy requirements and passive safety margins are most stringent during Operations, and less so during Standby. The transition between Manual to and from Standby also imposes unique requirements on the handling of mode transitions and performance, if the DSS is in acquisition or recovery (where the CDGNSS may not be available). Such mode-based operations mirror that seen in several recent or proposed missions such as VISORS [9, 10], mDOT [12, 13], and PROBA-3 [30].

II.2. Requirements Identification

This survey of contemporary and emerging distributed space missions Table 1 forms the foundation for identifying navigation flight software requirements that are both mission-relevant and broadly generalizable. By analyzing commonalities across mission objectives, operating baselines, and CDGNSS-based navigation methodologies, a unified set of requirements was distilled to guide the design of a robust and adaptable navigation architecture.

Requirements are segmented into Interfacing, Functional, and Performance in Table 4. The specification of interface and functional requirements implicitly assume an interface architecture depicted in Figure 2. Such a prescribed interface has been adopted for several missions that employ CDGNSS, such as PRISMA [1], Can-X 4/5 [7] [8], DWARF [36]. It is generalizable to future missions such as VISORS [10] and STARI [14] as well.

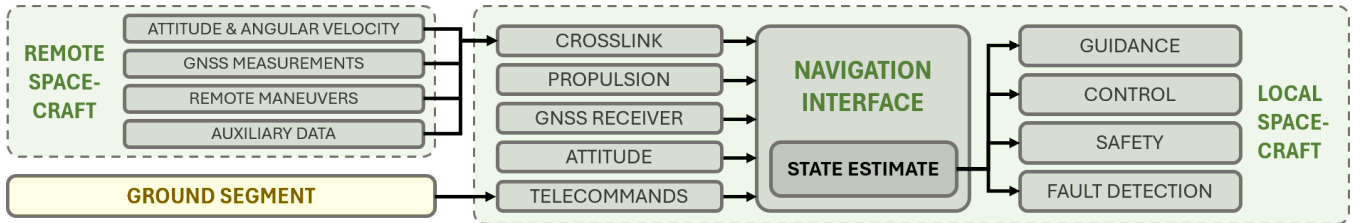


Figure 2: Assumed interface architecture applied in the context of identifying interface requirements.

The specification of performance requirements are segmented according to the types of navigation operations in Figure 3. These are derived from navigation requirements from each mode of Figure 1. The line mappings are a suggestive (and not prescriptive) indication on whether requirements for each form of navigation operation are being driven by mode requirements.

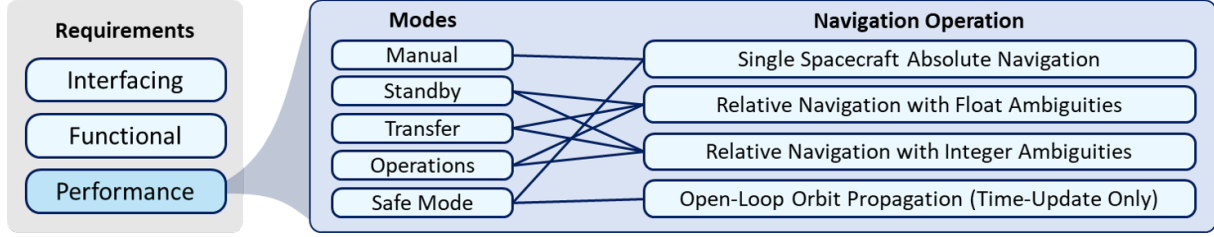


Figure 3: Mapping of navigation operating requirements to the spacecraft modes

	Interfacing Requirements	Parameter
R1.1	Local GNSS: Provide an interface for receiving local GNSS measurements at intervals τ_{meas} , GNSS ephemeris at intervals ≤ 2 hours, and receiver health data, with correct parsing and validation via checksums if applicable.	τ_{meas}
R1.2	Local Attitude: Provide an interface for receiving local attitude at intervals τ_{att} . If no angular velocity provided for propagation, then ≥ 2 attitude states are to be buffered for spherical linear inter/extrapolation over short arcs.	τ_{att}
R1.3	Local Propulsion: Provide an interface for receiving time-tagged local spacecraft maneuver plans to be buffered and applied during navigation filter time updates.	-
R1.4	Crosslink In/Out: Provide an interface for receiving crosslink <i>from</i> the remote spacecraft (and <i>to</i> , if the remote also executes onboard navigation), at intervals τ_{link} , with validation via checksums. Crosslink packets may include GNSS measurements, attitudes, maneuver plans, auxiliary data, status bytes, and state estimates if any.	τ_{link}
R1.5	Ground Segment: Provide an interface for receiving ground tele-commands <i>e.g.</i> filter configurations, mode-dependent parameters, and auxiliary data such as GPST leap seconds and Earth Orientation Parameters (EOPs).	-
R1.6	Outputs: Provide an interface to return or call-back to the host software with state estimates at intervals τ_{update} . If state estimates are anomalous, an incapability flag with status bytes should be returned instead.	τ_{update}
	Functional Requirements	
R2.1	State Covariance: Maintain the state estimate with a <i>positive-definite</i> covariance matrix that is reflective of the true state errors.	-
R2.2	State Dynamics Fidelity: Filter dynamics must provide sufficient fidelity in orbit perturbations without exceeding the margin of compute resources <i>i.e.</i> the filter time update and measurement update can be still be completed within τ_{update} , tested on a representative flight computer.	-
R2.3	Screening for Data Health: The flight software shall... <ul style="list-style-type: none"> Reject measurements with poor C/N_0 ratios. A recommended minimum value is 45 dB-Hz [37]. Reject local and remote maneuvers and measurements with outdated time-tags, with respect to filter time. Reject observed ranges and range rates with impossible magnitudes that lie outside expected bounds. Reject stale GNSS ephemerides (≥ 2 hours) or with bad Keplerian elements (<i>e.g.</i> negative eccentricity). Reject bad attitude state representations <i>e.g.</i> quaternions which violate unit norm constraints, and emit warning flags if attitudes received are not indicative of the pointing profile in the current mode. 	-
R2.4	Managing Telecommands and Telemetry: Navigation remains uninterrupted during telecommand uplink (<i>e.g.</i> filter tuning parameters, leap-second update, or new EOPs), and telemetry downlink.	-
R2.5	Managing Mode Switches: Navigation remains uninterrupted in the event of a system-wide role or mode switch. A handshake should be conducted between instances of the navigation flight software onboard and with remote spacecraft, if necessary, to prevent role or mode inconsistencies across the formation.	-
R2.6	Managing Measurement Latency: Provide a decision logic for transitioning to local-only spacecraft absolute state estimation, if an extended outage from the remote crosslink is experienced beyond some time horizon τ_{outage} . A decision logic for recovery back to precise relative state estimation should also be provided.	τ_{outage}
R2.7	Managing Attitude Latency: Propagate body-to-inertial attitude coordinates to the time-tag of the measurements at filter updates. If angular velocities are absent, perform a spherical linear inter/extrapolation instead [38].	-
R2.8	Fault Detection in Computations: Design against numerical instabilities. Automated unit tests throughout development are recommended. Potential problems include divisions by zero, negative eccentricities, square roots of negative real numbers, integer overflow or underflow, precision loss and ill-conditioned matrices. Functions to be checked include conversions of units, state representations, coordinate frames, time units and time scales.	-

R2.9	Cycle Slip Detection: Provide a mechanism for screening cycle slips (if the receiver does not already provide cycle slip flags), and reset estimated float ambiguities if a slip is indicated. Techniques common in literature include (i) consistency checks between the carrier phase and Doppler measurements, (ii) detection of discontinuities in double-differenced carrier phase, (iii) detection of impulses in triple-differenced carrier phase [37].	-
Performance Requirements		
R3.1	Absolute Navigation: Maintain a single-point positioning 1σ error of $\leq e_{abs}$ m and \dot{e}_{abs} m/s.	e_{abs}, \dot{e}_{abs}
R3.2	Relative Navigation (Pre-IAR): Maintain a relative positioning 1σ error of $\leq \delta e_{float}$ m and $\delta \dot{e}_{float}$ m/s at convergence of estimated single-differenced float ambiguities.	$\delta e_{float}, \delta \dot{e}_{float}$
R3.3	Relative Navigation (Post-IAR): Maintain a relative positioning 1σ error of $\leq \delta e_{iar}$ m and $\delta \dot{e}_{iar}$ m/s of single-differenced integer ambiguities using a $\geq 99\%$ probability of success metric.	$\delta e_{iar}, \delta \dot{e}_{iar}$
R3.4	Relative Navigation (Operations): In addition to R3.1 - R3.3, instrument or payload alignment requirements may be imposed along the longitudinal boresight axis of the instrument, or across the lateral plane perpendicular to the longitudinal, or both, given as the 1σ error δe_{lon} and δe_{lat} .	$\delta e_{lon}, \delta e_{lat}$
R3.5	Open-Loop Orbit Propagation: If state updates are necessary during measurement outages, then the open-loop propagation of the relative trajectory must be within an error tolerance of δe_{open} in the time horizon τ_{open} .	$\delta e_{open}, \tau_{open}$
R3.6	Robustness to Offset-from-Origin Biases: If there exists a poorly observable bias \vec{p} , between the chosen origin of the spacecraft body frame and the GNSS antenna phase center, then the performance requirements must be tolerant to the knowledge error of this bias given by $\Delta \vec{p}_{req}$.	$\Delta \vec{p}_{req}$
R3.7	Robustness to Over/Under-Actuation Maneuvers: Requirements R3.1 - R3.5 must remain satisfied in the event of over or under-actuation between the known maneuvers and true executed maneuvers up to some margin M_{man} .	M_{man}
R3.8	Robustness to Measurement Noise Variations: Requirements R3.1 - R3.5 must remain satisfied in the event of variations between modeled and actual measurement noise up to some margin M_{meas} . This variation is to be tested using a representative receiver under noise-configurable emulated GNSS signals.	M_{meas}

Table 4: Identified requirements of a generalized CDGNSS-based navigation flight software for DSS missions.

Deciding on the Interfacing and Functional requirement parameters in Table 4 may depend on the mission context and domain knowledge of other subsystems interfacing with navigation. τ_{meas} is limited by available observation rate of the GNSS receiver; τ_{att} is limited by the bus ADCS; τ_{link} is limited by crosslink availability; τ_{outage} requires domain knowledge on the expected crosslink latency; and while τ_{update} can be set as an ops requirement, it is also limited by τ_{meas} and τ_{link} . Deciding on the Performance requirements parameters requires a careful assessment of the navigation error tolerance necessary to meet mission-specific requirements.

An example of requirements parametrization is drawn from the VISORS mission: critical considerations for science observations are the focal length control accuracy, image drift rate, and attitude pointing accuracies, all during telescopic alignment. The science requirement is $\geq 20\%$ likelihood of success per observation attempt, and hence $\sim 99\%$ likelihood of ≥ 1 successful observation after 20 attempts [9, 10]. In total, these translate into overall Interfacing and Functional requirements parameters in Table 5 and Performance requirements parameters in Table 6, specific to the VISORS mission:

Table 5: Interfacing and Functional requirements drawn from the VISORS Navigation Flight Software

τ_{meas}	τ_{att}	τ_{link}	τ_{update}	τ_{outage}
10s	10s	10s	10s	4s

Table 6: Performance Requirements drawn from the VISORS Navigation Flight Software

\vec{e}_{abs}	$\dot{\vec{e}}_{abs}$	$\delta \vec{e}_{float}$	$\delta \dot{\vec{e}}_{float}$	$\delta \vec{e}_{int}$	$\delta \dot{\vec{e}}_{int}$	δe_{lon}	δe_{lat}	δe_{open}	τ_{open}	$\Delta \vec{p}_{req}$	M_{man}	M_{meas}
10m	0.03m/s	5cm	1mm/s	1cm	500 μ m/s	1.5cm	1.75cm	1m	1 orbit	5cm	$\pm 100\%$	$\pm 200\%$

II.3. Implications of Precision Requirements on the Receiver Phase Center and Spacecraft Attitude

Stringent precision requirements mandate consideration of the receiver antenna Phase Center Offset (PCO) from the body Center Of Mass (COM), and the directionally dependent Phase Center Variations (PCV). The PCO is the average point where GNSS signals are received from all signal directions, as opposed to the mechanical center [37]. The estimated positions of the spacecraft typically refer to the COM for ease of reference in orbit and attitude control.

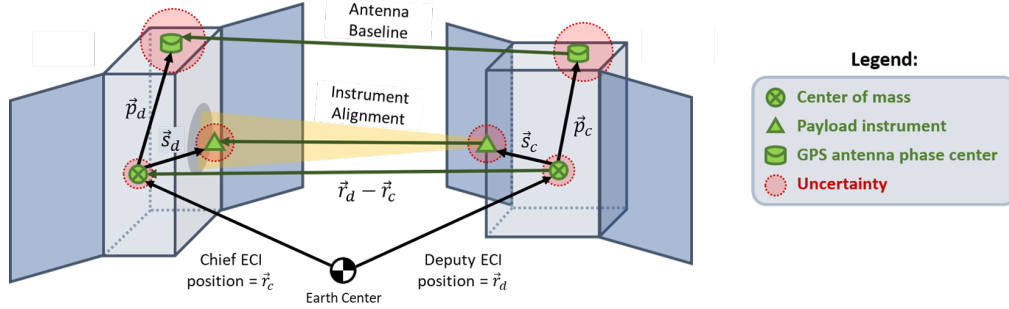


Figure 4: Illustration of body-frame component position uncertainties in the VISORS spacecraft (Source: [10]).

However, GNSS measurements are observed at the PCO. Hence, the only observable point in the body frame through GNSS measurements is the PCO, whereas the COM has poor observability, as per Figure 4. The components of the COM-to-PCO vector \vec{p} are hence poorly observable, but must be accounted for in modeled CDGNSS measurements [39]. A known *a priori* vector \vec{p}_{static} from the body origin to a static antenna center is typically recorded from a mechanical model as an initial guess. Then \vec{p} is modeled in body-frame coordinates as

$$\vec{p} = \vec{p}_{static} + \Delta\vec{p} \quad (1)$$

where $\Delta\vec{p}$ is assumed zero-mean Gaussian with cm-level uncertainty. Ground calibration of the PCO and PCV in an anechoic chamber may reduce uncertainty. However, calibration campaigns may be infeasible if the system integrator lacks the facilities and resources. Often, DSS pathfinder missions employ cost-efficient platforms *i.e.* CubeSats [1, 6, 7, 8, 9, 10, 14] using commercial grade components with limited calibration. Even with calibration, time-varying uncertainties in COM-to-PCO evolve in flight. For instance, non-rigid body dynamics (solar panels, fuel slosh etc) contribute to an evolving COM, while signal-in-space conditions introduce time-varying effects on the PCO. Recent work suggests that highly agile attitude maneuvers improve the observability of $\Delta\vec{p}$ if estimated directly via state augmentation [40]. However, this assumes a static COM-to-PCO. Furthermore, frequent attitude calibration maneuvers may be infeasible if attitude profiles are restricted.

Therefore, it is necessary to account for the influence of COM-to-PCO bias errors on navigation precision within the filter. Error budgeting of body-frame bias errors in DSS are not commonly considered in literature. An exception is the proposed Cal X-1 mission [41]. Such accounting can be pursued in two ways. First, additive or multiplicative measurement underweighting is one recommended practice in literature [42, 43]. Second, treating bias errors as Consider parameters [44] using a Consider Kalman Filter [45, 46] could accurately incorporate their uncertainties into the full state covariance. This reduces filter over-confidence, prevent larger-than-expected prefit residuals, and hence protect against trigger filter divergence [47]. This is a critical motivation behind the choice of adopting the Consider Kalman Filter in Section III.

Accounting for \vec{p} in the measurement model requires minimizing latency between the body-to-inertial attitude time and the filter time, as per R2.7. This minimizes contributions to residuals due to the uncompensated lever arm motion of \vec{p} . A simple Euler step as per Equation 2 can mitigate much of the error. Let the last known attitude packet at time t_{att} be the set $[\omega(t_{att}), \mathbf{q}(t_{att})]$, where $\mathbf{q}(t_{att})$ is the body-to-inertial quaternion and $\omega(t_{att})$ is the body-to-inertial angular velocity expressed in the body frame. Then, let $\Delta t_{att} \in \mathbb{R}$ be the difference between the current filter time and t_{att} ,

$$\mathbf{q}(t_{att} + \Delta t_{att}) = \delta\mathbf{q} \otimes \mathbf{q}(t_{att}), \quad \delta\mathbf{q} = \begin{bmatrix} \cos\left(\frac{1}{2} \|\omega(t_{att})\| \Delta t_{att}\right) \\ \hat{\omega} \sin\left(\frac{1}{2} \|\omega(t_{att})\| \Delta t_{att}\right) \end{bmatrix} \quad (2)$$

where $\hat{\omega} \in \mathbb{R}^3$ is the normalized direction of $\omega(t_{att})$ and \otimes is the quaternion multiplier. If angular velocity data is absent, one may instead do quaternion interpolation *i.e.* SLERP [38], as was implemented for the PRISMA mission [1].

III. NAVIGATION FUNCTIONAL ARCHITECTURE

III.1. Overview of Architecture

The navigation architecture builds on the DiGiTaL flight software [20, 21], with heritage from PRISMA [6, 25], and is hereafter referred to as DiGiTaL v2. Absolute position estimation uses Group and Phase Ionospheric Calibration (GRAPHIC) measurements [48], which combine pseudorange and Zero-Difference Carrier Phase (ZDCP) to mitigate ionospheric errors. Relative baseline estimation uses Single-Difference Carrier Phase (SDCP) measurements shared over a crosslink. The architecture in Figure 5 comprises four blocks: (i) the data interface, (ii) navigation filter, (iii) IAR, and (iv) FDIR.

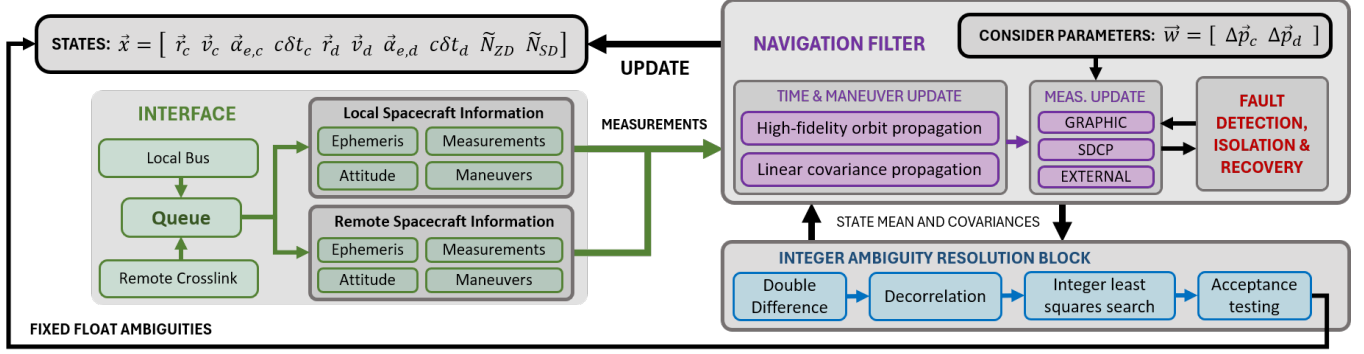


Figure 5: Navigation functional architecture based on CDGNSS with IAR, for a two-spacecraft state vector

The default state vector per spacecraft contains the inertial position \vec{r}_i and velocity \vec{v}_i of the spacecraft COM, empirical accelerations $\vec{\alpha}_{e,i}$, and receiver clock offsets $c\delta t_i$. 48 channels total are set aside for estimating ZDCP and SDGP float ambiguities \tilde{N}_{ZD} and \tilde{N}_{SD} . Receiver clock offsets and empirical accelerations are modeled temporally as first-order Gauss-Markov processes. Receiver clock offsets are prescribed an infinite time constant, describing a random walk. For a two-spacecraft formation involving a chief (c) and deputy (d), the states \vec{x} and consider states \vec{w} are in Equation 3,

$$\vec{x} = [\vec{r}_c, \vec{v}_c, \vec{\alpha}_{e,c}, c\delta t_c, \vec{r}_d, \vec{v}_d, \vec{\alpha}_{e,d}, c\delta t_d, \tilde{N}_{ZD}, \tilde{N}_{SD}] \quad , \quad \vec{w} = [\Delta \vec{p}_c, \Delta \vec{p}_d] \quad (3)$$

where $\vec{x} \in \mathbb{R}^{68}$ and $\vec{w} \in \mathbb{R}^6$ for two-spacecraft. The flushing of estimated ambiguities to the rear of the state vector in Equation 3 is a deliberate design choice with important implications for optimizing computational efficiency later on in Section V. The full covariance block structure with the consider parameters is as per Equation 4, where $\Sigma^{(x)}$ are state covariances; $\Sigma^{(w)}$ are consider covariances; $\Sigma^{(xw)} = \Sigma^{(wx)\top}$ are the cross-covariances between states and consider parameters,

$$\Sigma = \begin{bmatrix} \Sigma^{(x)} & \Sigma^{(xw)} \\ \Sigma^{(wx)} & \Sigma^{(w)} \end{bmatrix} \quad (4)$$

III.2. Stable and Regularized Consider Extended Kalman Filter

The Extended Kalman Filter (EKF) has had flight-proven success with many best practices accumulated [43, 49]. The Consider EKF (CEKF) incorporates the Consider Parameters into the state covariance [44, 45], but the typical minimum covariance form [46] can pose numerical stability issues, detrimental to real-time flight use. This section modifies the CEKF into a Positive-Definite (PD) preserving Joseph-like form, which has not been presented in literature to the best of the authors' knowledge. Regularization of the innovation covariance is introduced to ensure PD. Key modifications are in Equation 12 and Equation 18. The time update follows the minimum covariance form, except that \vec{w} is static in the body-frame, and hence no state transitions,

$$\vec{x}_{t|t-1} = f(\Delta t, \vec{x}_{t-1|t-1}, \mathbf{M}) \quad (5)$$

$$\Sigma_{t|t-1}^{(x)} = \Phi_{t-1}^\top \Sigma_{t-1|t-1}^{(x)} \Phi_{t-1} + \mathbf{Q}_t \quad (6)$$

$$\Sigma_{t|t-1}^{(xw)} = \Sigma_{t|t-1}^{(wx)\top} = \Phi_{t-1}^\top \Sigma_{t-1|t-1}^{(xw)} \quad (7)$$

where f is a non-linear orbit propagator function with higher order perturbations included; $\mathbf{M} \in \mathbb{R}^{r \times 3}$ is a maneuver buffer of size r expressed in an appropriate reference frame; Φ_{t-1} is the State Transition Matrix (STM) at time $t-1$; and \mathbf{Q}_t is the

process noise matrix at time t . An analytical form of Φ_{t-1} is difficult to achieve in practice, and hence an approximated STM can be computed using the variational equations so as to capture perturbations of f in the STM. This is reviewed in Chapter 7 of Montenbruck and Gill [50]. The estimated empirical accelerations are then updated by the decay constant of a Gauss-Markov process of first order in Equation 8, and the attitudes are propagated to match the current filter time in Equation 9,

$$\vec{\alpha}_{e,i} = \vec{\alpha}_{e,i} \cdot e^{\Delta t / \tau_{\alpha e}}, \quad \forall i \quad (8)$$

$$\mathbf{q}(t) = \delta \mathbf{q} \otimes \mathbf{q}(t_{att}), \quad \text{see Equation 2} \quad (9)$$

where $\mathbf{q}(t_{att})$ is the last known attitude at ADCS time t_{att} . Attitude time-tags t_{att} marked by the ADCS must also be converted to the same time scale as the filter *i.e.* GPST. Next, the measurement update steps are presented. Given an observed measurement of size m \vec{z}_t , the innovation, or prefit residual, $\vec{v}_t \in \mathbb{R}^m$ is

$$\vec{v}_t = \vec{z}_t - h(\vec{x}_{t|t-1}, \vec{w}_{t|t-1}, \mathbf{q}(t)) \quad (10)$$

where $\vec{x}_{t|t-1} \in \mathbb{R}^n$, $\vec{w}_{t|t-1} \in \mathbb{R}^\ell$, and $h : \mathbb{R}^{n+\ell} \times \mathbb{H} \rightarrow \mathbb{R}^m$ is the non-linear measurement model; then $\mathbf{H}_t^{(x)} \in \mathbb{R}^{m \times n}$ and $\mathbf{H}_t^{(w)} \in \mathbb{R}^{m \times \ell}$ are the first-order measurement sensitivities with respect to states \vec{x} and consider parameters \vec{w} ; $\mathbf{R}_t \in \mathbb{R}^{m \times m}$ is the modeled measurement covariance at t , positive definite at construction. A review of GRAPHIC and SDCP models can be found in the references [1, 21, 37, 48]. The innovation covariance, with consider parameters \vec{w} included, is expressed as

$$\mathbf{V}_t = \underbrace{\mathbf{H}_t^{(x)} \Sigma_{t|t-1}^{(x)} \mathbf{H}_t^{(x)\top}}_{\text{positive definite form}} + \underbrace{\mathbf{H}_t^{(x)} \Sigma_{t|t-1}^{(xw)} \mathbf{H}_t^{(w)\top} + \mathbf{H}_t^{(w)} \Sigma_{t|t-1}^{(wx)} \mathbf{H}_t^{(x)\top}}_{\text{not guaranteed positive definite}} + \underbrace{\mathbf{H}_t^{(w)} \Sigma_{t|t-1}^{(w)} \mathbf{H}_t^{(w)\top}}_{\text{positive definite form}} + \mathbf{R}_t \quad (11)$$

where it must be noted that in Equation 11, the sum of two terms, while symmetric, is *not guaranteed* PD theoretically. In practice, this is compounded by numerical errors from finite precision and rounding accumulated over time. Hence, the innovation covariance \mathbf{V}_t for the conventional CEKF is *also not guaranteed* PD, which means its inverse may not exist. Since the optimal Kalman gain \mathbf{K}_t scales inversely with the uncertainty of the innovation, as in Equation 12,

$$\mathbf{K}_t = \left(\Sigma_{t|t-1}^{(x)} \mathbf{H}_t^{(x)\top} + \Sigma_{t|t-1}^{(xw)} \mathbf{H}_t^{(w)\top} \right) (\mathbf{V}_t + \bar{\mathbf{V}})^{-1} \quad (12)$$

a catastrophic singularity may occur mid-flight if the inverse does not exist. In light of this, regularizing the innovation with an extra term $\bar{\mathbf{V}}$ is proposed, in order to guarantee the existence of the inverse in Equation 12. The existence of $\bar{\mathbf{V}}$ ensures that the sum $\mathbf{H}_t^{(x)} \Sigma_{t|t-1}^{(xw)} \mathbf{H}_t^{(w)\top} + \mathbf{H}_t^{(w)} \Sigma_{t|t-1}^{(wx)} \mathbf{H}_t^{(x)\top} + \bar{\mathbf{V}}$ is always PSD, so that $\mathbf{V}_t + \bar{\mathbf{V}}$ is PD and hence invertible. The construction of $\bar{\mathbf{V}}$ that makes the smallest possible adjustment to the terms within the inverse in Equation 12, as measured by the trace, can be found as follows. First, the sum of matrices that is non-guaranteed PD is real and symmetric and hence diagonalizable,

$$\Psi \Lambda \Psi^\top = \text{eig} \left(\mathbf{H}_t^{(x)} \Sigma_{t|t-1}^{(xw)} \mathbf{H}_t^{(w)\top} + \mathbf{H}_t^{(w)} \Sigma_{t|t-1}^{(wx)} \mathbf{H}_t^{(x)\top} \right) \quad (13)$$

Then, for diagonal indices $i \in [1, m]$ along Λ , where m is the number of measurements, if a negatively valued λ_i is found, the corresponding value of γ_i is set to $-\lambda_i$; otherwise, it is set to zero since the eigenvalues are already positive,

$$\bar{\mathbf{V}} = \Psi \cdot \text{diag}([\gamma_1, \gamma_2, \dots, \gamma_m]) \cdot \Psi^\top \quad \text{where } \gamma_i = \max(0, -\lambda_i) \text{ and } \lambda_i \text{ are diagonals of } \Lambda \quad (14)$$

thereby ensuring that $\Psi \Lambda \Psi^\top + \bar{\mathbf{V}}$ will have only non-negative eigenvalues. In practice, eigen-decomposition at each measurement update is costly for flight. Assuming independent measurements, often valid for GNSS [37], will simplify 13 to 14. Measurements can then be processed sequentially as scalars ($m = 1$). Hence, $\bar{\mathbf{V}} \in \mathbb{R}$, and Equation 14 simplifies to:

$$\bar{\mathbf{V}} = \max \left(0, - \left(\mathbf{H}_t^{(x)} \Sigma_{t|t-1}^{(xw)} \mathbf{H}_t^{(w)\top} + \mathbf{H}_t^{(w)} \Sigma_{t|t-1}^{(wx)} \mathbf{H}_t^{(x)\top} \right) \right) \quad (\text{scalar}) \quad (15)$$

The measurement update of the *a posteriori* state mean then applies the sub-optimal Kalman gain in the linear update,

$$\vec{x}_{t|t} = \vec{x}_{t|t-1} + \mathbf{K}_t \vec{v}_t \quad (16)$$

Then, the Joseph-like form measurement update guarantees the *a posteriori* state covariance in Equation 18 is PD,

$$\mathbf{U}_t = \left[[\mathbf{K}_t \mathbf{H}_t^{(x)} - \mathbf{I}_{n \times n}], [\mathbf{K}_t \mathbf{H}_t^{(w)}] \right] \quad (17)$$

$$\Sigma_{t|t}^{(x)} = \mathbf{U}_t \Sigma_{t|t-1} \mathbf{U}_t^\top + \mathbf{K}_t \mathbf{R}_t \mathbf{K}_t^\top \quad (\text{preserves positive definiteness}) \quad (18)$$

$$\Sigma_{t|t}^{(xw)} = (\mathbf{I}_{n \times n} - \mathbf{K}_t \mathbf{H}_t^{(x)}) \Sigma_{t|t-1}^{(xw)} - \mathbf{K}_t \mathbf{H}_t^{(w)} \Sigma^{(w)} \quad (19)$$

The Joseph-like form for the CEKF can be derived by performing a matrix factorization using \mathbf{U}_t in Equation 17, without substitution of the optimality condition. This enables the uncertainty from poorly observed consider parameters \vec{w} , the COM-to-PCO biases, to propagate and be reflected into the state covariance [R2.1].

An important *trade-off*, however, is that in the Joseph-like form, most terms are dense, and hence sparse matrix operations cannot be fully exploited for speed, in exchange for numerical stability.

III.3. Process Noise Modeling

To meet requirements across all modes (Figure 3), including during outages, the process noise model \mathbf{Q}_t must capture orbit propagation uncertainties and unmodeled dynamics while preserving state correlation structures. Accurate modeling of correlations is critical not only for estimation when measurements are available, but also for orbit prediction during data gaps [43, 51, 52]. Empirical accelerations are included as stochastic states and modeled spatially and temporally using first-order Gauss-Markov processes in the Radial-Tangential-Normal (RTN) frame, enabling directional decoupling of effects such as drag, solar radiation pressure, higher-order gravity, and maneuvers. When the spectral noise density accurately reflects these correlations, the resulting process noise preserves them appropriately. An exponential spatial correlation model is adopted to capture inter-spacecraft dynamics coupling. In Equation 20, $\beta_{ij} = \exp(-d_{ij}/D_0)$ encodes the correlation between spacecraft i and j as a function of their separation d_{ij} , with D_0 as a tunable correlation length scale.

$$\beta_{ij} = \exp(-d_{ij}/D_0) \quad (20)$$

This model represents a first-order Gauss-Markov process with spatial correlation, commonly used in Gaussian process modeling [53]. It captures the intuition that dynamics of nearby spacecraft are more strongly correlated than those farther apart. Consequently, the spectral noise density matrices for individual and joint spacecraft dynamics, \mathbf{S}_α and $\mathbf{S}_\alpha^{(ij)}$, are defined as

$$\mathbf{S}_\alpha^{(ij)} \equiv \begin{bmatrix} \mathbf{S}_\alpha & \beta_{ij} \mathbf{S}_\alpha \\ \beta_{ij} \mathbf{S}_\alpha & \mathbf{S}_\alpha \end{bmatrix}, \text{ where } \mathbf{S}_\alpha \equiv \text{diag} \left(\begin{bmatrix} \sigma_R & \sigma_T & \sigma_N \end{bmatrix} \right) \quad (21)$$

and both \mathbf{S}_α and D_0 are user-defined. The joint process noise covariance for the Cartesian states of spacecraft i and j , denoted $\mathbf{Q}_{rv\alpha}$, is analytically derived by mapping the spectral noise density onto the Cartesian states via the process noise mapping matrix $\Gamma(\tau)$, and propagating it through the Cartesian state transition matrix $\Phi_{rv\alpha}(t, \tau)$ [54], as shown in Equation 22. If the STM is integrable and across a short time interval Δt , Equation 22 can be approximated in Equation 23,

$$\mathbf{Q}_{rv\alpha} = \int_{t_0}^t \Phi_{rv\alpha}(t, \tau) \cdot \Gamma(\tau) \cdot \mathbf{S}_\alpha^{(ij)} \cdot \Gamma(\tau)^\top \cdot \Phi_{rv\alpha}(t, \tau)^\top d\tau \quad (22)$$

$$\approx \Phi_{rv\alpha}(t, t + \Delta t) \cdot \Gamma(\Delta t) \cdot \mathbf{S}_\alpha^{(ij)} \cdot \Gamma(\Delta t)^\top \cdot \Phi_{rv\alpha}(t, t + \Delta t)^\top \quad (23)$$

The Cartesian state joint STM for spacecraft i and j , $\Phi_{rv\alpha}$, can be evaluated through numerical integration of the variational equations [1, 21, 50]. $\Phi_{rv\alpha}$ is organized in block form for a two-spacecraft joint state i and j as

$$\Phi_{rv\alpha} = \begin{bmatrix} \Phi_{rv\alpha}^{(i)} & \mathbf{0}_{9 \times 9} \\ \mathbf{0}_{9 \times 9} & \Phi_{rv\alpha}^{(j)} \end{bmatrix}, \text{ where } \Phi_{rv\alpha}^{(i)} = \begin{bmatrix} \Phi_{rv}^{(i)} & \Phi_{rv,\alpha}^{(i)} \\ \mathbf{0}_{3 \times 6} & \Phi_\alpha^{(i)} \end{bmatrix} \text{ and } \Phi_{rv\alpha}^{(j)} = \begin{bmatrix} \Phi_{rv}^{(j)} & \Phi_{rv,\alpha}^{(j)} \\ \mathbf{0}_{3 \times 6} & \Phi_\alpha^{(j)} \end{bmatrix} \quad (24)$$

Care must be taken to ensure that the states are represented in the correct coordinate frames. In the two-spacecraft state vector of Equation 3, positions and velocities are in Earth-Centered Inertial (ECI) frame, while empirical accelerations are in RTN frame. Let the RTN-to-ECI rotation be $\begin{bmatrix} ECI \mathbf{R}_{RTN}^{(i)} \end{bmatrix} \in \mathbb{R}^{3 \times 3}$, and let $[\omega^\times]$ be the angular velocity of RTN with respect to ECI,

expressed in skew-symmetric form, in the RTN basis. Then, the coordinate frame mapping matrix of spacecraft i is

$$\mathbf{C}^{(i)} = \begin{bmatrix} \begin{bmatrix} ECI\mathbf{R}_{RTN}^{(i)} \\ ECI\mathbf{R}_{RTN}^{(i)} \end{bmatrix} [\omega^\times] & \mathbf{0}_{3 \times 3} & \mathbf{0}_{3 \times 3} \\ \mathbf{0}_{3 \times 3} & \mathbf{0}_{3 \times 3} & \mathbf{I}_{3 \times 3} \end{bmatrix} \quad (25)$$

Empirical accelerations are also modeled as first-order Gauss-Markov random processes correlated *in time* [1, 21, 43, 55], where present estimates of empirical accelerations are modeled to be correlated with past estimates in an exponentially decaying manner. The time decay constant θ , with τ_0 being a user-defined correlation time scale, and with elapsed time Δt , is

$$\theta = \exp(-\Delta t/\tau_0) \quad (26)$$

Therefore, the joint-spacecraft process noise mapping matrix $\mathbf{\Gamma}$ for spacecraft i and j over a time interval Δt is simply

$$\mathbf{\Gamma}(\Delta t) = \begin{bmatrix} \mathbf{C}^{(i)}\tilde{\mathbf{\Gamma}}(\Delta t) & \mathbf{0}_{9 \times 3} \\ \mathbf{0}_{9 \times 3} & \mathbf{C}^{(j)}\tilde{\mathbf{\Gamma}}(\Delta t) \end{bmatrix}, \quad \text{where} \quad \tilde{\mathbf{\Gamma}}(\Delta t) = \begin{bmatrix} \frac{1}{2}\Delta t^2 \cdot \mathbf{I}_{3 \times 3} \\ \Delta t \cdot \mathbf{I}_{3 \times 3} \\ (1 - \theta^2) \cdot \mathbf{I}_{3 \times 3} \end{bmatrix} \quad (27)$$

The analytical process noise can now be evaluated by substituting 25 and 26 into 27, and then 21, 24, 27 into 23,

$$\mathbf{Q}_{rv\alpha} = \begin{bmatrix} \mathbf{Q}_{rv\alpha}^{(i)} & \mathbf{Q}_{rv\alpha}^{(ij)} \\ \mathbf{Q}_{rv\alpha}^{(ji)} & \mathbf{Q}_{rv\alpha}^{(j)} \end{bmatrix} \quad (28)$$

$$\begin{aligned} \mathbf{Q}_{rv\alpha}^{(i)} &= \mathbf{\Phi}^{(i)} \cdot \mathbf{C}^{(i)} \cdot \tilde{\mathbf{\Gamma}}(\Delta t) \cdot \mathbf{S}_\alpha \cdot \tilde{\mathbf{\Gamma}}(\Delta t)^\top \cdot \mathbf{C}^{(i)\top} \cdot \mathbf{\Phi}^{(i)\top} \\ \text{where} \quad \mathbf{Q}_{rv\alpha}^{(j)} &= \mathbf{\Phi}^{(j)} \cdot \mathbf{C}^{(j)} \cdot \tilde{\mathbf{\Gamma}}(\Delta t) \cdot \mathbf{S}_\alpha \cdot \tilde{\mathbf{\Gamma}}(\Delta t)^\top \cdot \mathbf{C}^{(j)\top} \cdot \mathbf{\Phi}^{(j)\top} \\ \mathbf{Q}_{rv\alpha}^{(ij)} &= \mathbf{Q}_{rv\alpha}^{(ji)\top} = \mathbf{\Phi}^{(i)} \cdot \mathbf{C}^{(i)} \cdot \tilde{\mathbf{\Gamma}}(\Delta t) \cdot (\beta_{ij}\mathbf{S}_\alpha) \cdot \tilde{\mathbf{\Gamma}}(\Delta t)^\top \cdot \mathbf{C}^{(j)\top} \cdot \mathbf{\Phi}^{(j)\top} \end{aligned} \quad (29)$$

The full process noise matrix for the two-spacecraft state vector of Equation 3, including receiver clock biases tracked for k GNSS constellations, and c channels each for ZDCP and SDCP float ambiguities, is expressed as,

$$\mathbf{Q}_t = \begin{bmatrix} \mathbf{Q}_{rv\alpha}^{(i)} & \mathbf{0}_{9 \times k} & \mathbf{Q}_{rv\alpha}^{(ij)} & \mathbf{0}_{9 \times k} & \mathbf{0}_{9 \times c} & \mathbf{0}_{9 \times c} \\ \mathbf{0}_{k \times 9} & \mathbf{Q}_{c\delta t}^{(i)} & \mathbf{0}_{k \times 9} & \mathbf{0}_{k \times k} & \mathbf{0}_{k \times c} & \mathbf{0}_{k \times c} \\ \mathbf{Q}_{rv\alpha}^{(ji)} & \mathbf{0}_{9 \times k} & \mathbf{Q}_{rv\alpha}^{(j)} & \mathbf{0}_{9 \times k} & \mathbf{0}_{9 \times c} & \mathbf{0}_{9 \times c} \\ \mathbf{0}_{k \times 9} & \mathbf{0}_{k \times k} & \mathbf{0}_{k \times 9} & \mathbf{Q}_{c\delta t}^{(j)} & \mathbf{0}_{k \times c} & \mathbf{0}_{k \times c} \\ \mathbf{0}_{c \times 9} & \mathbf{0}_{c \times k} & \mathbf{0}_{c \times 9} & \mathbf{0}_{c \times k} & \mathbf{Q}_{N_{ZD}} & \mathbf{0}_{c \times c} \\ \mathbf{0}_{c \times 9} & \mathbf{0}_{c \times k} & \mathbf{0}_{c \times 9} & \mathbf{0}_{c \times k} & \mathbf{0}_{c \times c} & \mathbf{Q}_{N_{SD}} \end{bmatrix} \quad (30)$$

This analytical process noise model preserves the spatial and temporal correlation structure of the Cartesian states, as implied by the spectral density \mathbf{S}_α^{ij} . It also removes the need for manual tuning of position and velocity noise parameters, offering a physically grounded approach aligned with the filter's estimate of required dynamic noise compensation. As shown in Section VI, this yields substantial improvements in state prediction accuracy during GNSS-denied intervals compared to the previous DiGiTaL implementation.

III.4. Measurement Noise Modeling

The measurement noise model \mathbf{R}_t is vital for influencing how the filter weighs observations relative to predicted states. Inaccurate modeling may lead to erroneous state estimates and cause discrepancies between the state covariance and true state error. Since correlated measurement biases are canceled in the GRAPHIC and SDCP measurements, while remaining biases are actively estimated in the state, the filter is primarily concerned with accurate modeling of the thermal noise contributions.

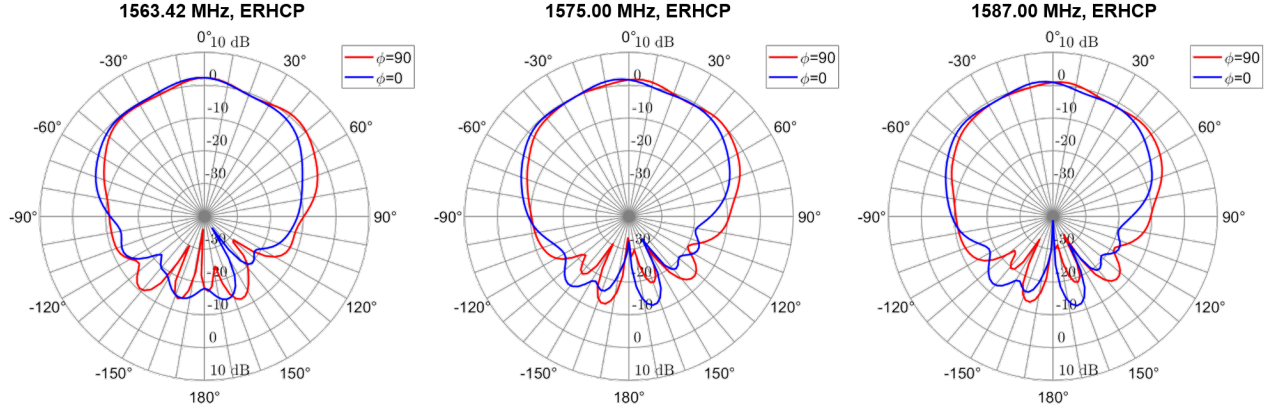


Figure 6: Calibrated antenna gain pattern of the Model 1.9G1215P-12S-2-OSR, with antenna orientation ϕ (Credits: ANTCOM)

This section outlines the process of thermal noise modeling, using a Novatel OEM628 GNSS receiver, and an ANTCOM 1.9G1215P antenna, as working examples. Both units are near-identical representations of the flight units onboard the VISORS spacecraft, with flight heritage. The antenna gain pattern is made available to the flight software via a parametric fit of the actual calibrated data, as seen in Figure 6. Antenna gain values can be sampled from a parametric fit based on the elevation-azimuth. The Carrier-to-Noise Ratio C_{N_0} can be computed through a link budget for various elevation angles in Table 7,

Table 7: Link budget analysis and thermal noise tabulation for the Novatel OEM628 and an ANTCOM 1.9G1215P antenna, at GPS L1 $f = 1575.42$ MHz. Elevation is measured from the antenna plane. Free space path loss assumes a fixed slant range of 20,000km. Carrier signal strength (C) [dBW] is the sum of gains and losses from the antenna, receiver, GPS transmitter, and the free space path.

		Zenith	Roll-Off	Horizon	Nadir
Elevation	(\cdot) $^\circ$	90	60	0	-90
Antenna Gain	dBW	1.7	-0.6	-10.9	-15.0
Receiver LNA Gain	dBW	30.0			
Receiver Circuit Loss	dBW	-1.0			
Receiver Polarization Loss	dBW	-3.0			
GPS Antenna Gain	dBW	13.5			
GPS Transmit Power	dBW	14.25			
GPS Transmit Loss	dBW	-1.25			
Free Space Path Loss	dBW	-182.419			
Atmospheric Losses	dBW	-0.10			
Noise Spectral Density (N_0)	dBW/Hz	-169.919			
Carrier Signal Strength (C)	dBW	-125.3185	-127.6185	-137.9185	-142.0185
Carrier-to-Noise Ratio (C_{N_0})	dBW \cdot Hz	41.7	39.4	29.1	25.0
Pseudorange Thermal Noise σ_ρ	m	0.149	0.194	0.634	1.016
Carrier Phase Thermal Noise σ_ϕ	mm	0.682	0.887	2.909	4.664

The signal-to-noise ratio S_{NR} relates to C_{N_0} [dB-Hz] via a log-to-linear scale conversion $S_{NR} = 10^{C_{N_0}/10}$. An analytical thermal noise model formulated by Psiaki and Mohiuddin [39] for undifferenced carrier phase σ_ϕ in Equation 31 and raw pseudorange σ_ρ in Equation 32 is referenced below for convenience,

$$\sigma_\phi = \frac{\lambda}{2\pi} \sqrt{\frac{B_{PLL}}{2S_{NR}}} \quad [\text{meters}] \quad (31)$$

$$\sigma_\rho = ct_c \sqrt{\frac{B_{DLL} t_{eml}}{2t_c S_{NR}}} \left(1 + \frac{1}{t_{acc} S_{NR}} \right) \quad [\text{meters}] \quad (32)$$

where B_{PLL} and B_{DLL} are the receiver loop bandwidths for the receiver Phase-Lock Loop (PLL) and Delay-Lock Loop (DLL) respectively; t_{eml} denotes the early-minus-late correlator spacing in seconds; t_{acc} refers to the pre-detection integration time over which signal energy is accumulated before discriminator evaluation; $t_c = 1/f_c$ is the chipping period of the pseudorandom code, where $f_c = 1.023$ MHz for GPS L1 C/A; c and λ are the speed of light and wavelength. Typically, B_{PLL} and B_{DLL} may be disclosed by the manufacturer, but often, very specific design parameters such as t_{eml} and t_{acc} may not be. In the case of the Novatel OEM628, $B_{DLL} = 0.0076$ Hz and $B_{PLL} = 15$ Hz. It is assumed that $t_{eml} = 1$ -chip period, which is reasonable for modern receivers, and that the accumulation interval t_{acc} is sufficiently long so that $t_{acc}S_{NR} \gg 1$. This simplifies the pseudorange thermal noise model to Equation 33,

$$\sigma_\rho \approx \frac{c}{f_c} \sqrt{\frac{B_{DLL}}{2S_{NR}}} \quad [\text{meters}] \quad (33)$$

The filter may then discern thermal noise 31 and 33 using a look-up table of the antenna gain values, which are in turn based on the azimuth-elevation of the arriving signal.

III.5. Integer Ambiguity Resolution

The topic of IAR is well-researched in literature. Hence, the IAR module, based on the Modified LAMBDA algorithm [2, 56] is only briefly outlined here, for the completion of the full presentation, with its functional diagram in Figure 7.

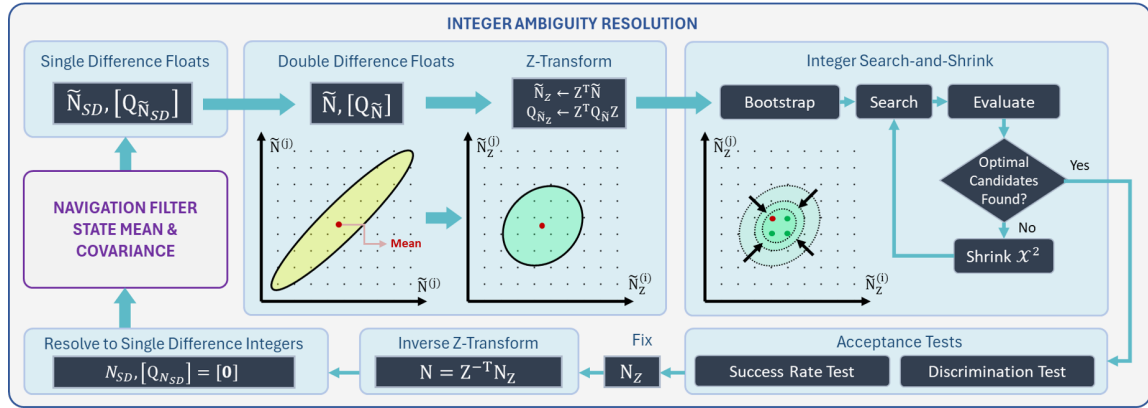


Figure 7: Block diagram of the Integer Ambiguity Resolution (IAR) block, expanded from Figure 5.

First, SDCP floats \tilde{N}_{SD} are double-differenced to DDCP floats \tilde{N} . Components of the \tilde{N} vector are highly correlated due to the common SDCP reference measurement. Decorrelation using the integer-preserving Z-transform [2] reduces the size of the search space prior to integer search. The Z-transform matrix Z is an integer approximation of the lower triangular matrix L , which comes from the $Q_{\tilde{N}} = LDL^T$ decomposition. Z is derived by imposing the integer constraints given in [57], so that

$$Q_{\tilde{N}_z} = Z^T LDL^T Z \approx D \quad (34)$$

The Z-transformed DDCP float ambiguities $\tilde{N}_z = Z^T \tilde{N}$. The result is a transformed mean \tilde{N}_z and covariance $Q_{\tilde{N}_z}$ that is almost decorrelated, though not completely due to the integer constraints. The initial guess of integer candidates is done via recursive conditional rounding [58]. The rounded integers allow bounding of the initial search width in the discrete integer space, which is successively shrunk during integer search to minimize the computational costs of evaluating sub-optimal candidates. For each integer candidate N_z , the integer least squares objective function to minimize over all candidates is

$$\min_{N_z} \|N_z - \tilde{N}_z\|_{Q_{\tilde{N}_z}^{-1}}^2 \quad (35)$$

When the best candidate can no longer be improved, it is only resolved into an integer if it passes recommended acceptance tests, such as the Success Rate and Discrimination Tests [58], or meets an Ambiguity Dilution of Precision (ADOP) [59] threshold. This paper adopts the Success Rate Test with a 99% threshold and the Discrimination Test.

IV. NAVIGATION FAULT DETECTION, ISOLATION, AND RECOVERY

The Fault Detection, Isolation, and Recovery (FDIR) module is designed to ensure continuous and robust navigation against anomalous measurements. Three key sub-functions of FDIR are highlighted in red in the functional architecture of Figure 8,

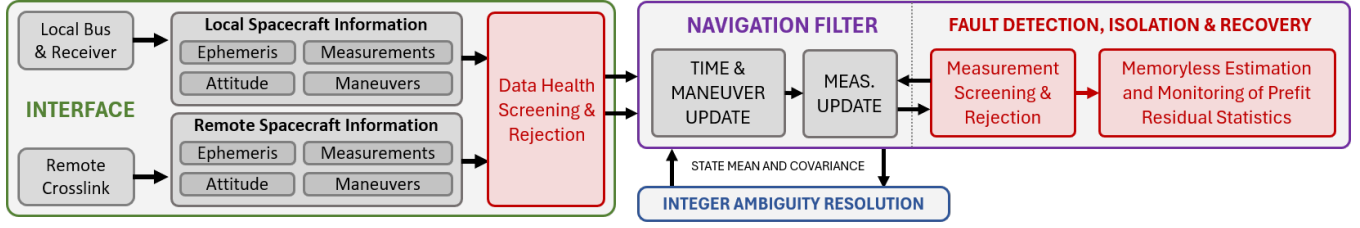


Figure 8: Functional architecture of the Fault Detection Isolation and Recovery (FDIR) block, expanded from Figure 5.

IV.1. Data Health Screening and Rejection

The health of incoming measurements, maneuvers, attitudes, ephemerides, and telecommands are screened for validity. Packet headers and checksums are inspected. Sanity checks are conducted *e.g.* unexpectedly low or high pseudorange, carrier phase, C/N_0 values etc; bad GNSS ephemeris values; time-relevance of maneuvers or measurements in-the-past etc. This includes local (bus) and remote (through crosslink) data. These first-layer checks ensure data integrity down the signal chain in subsequent modules, thereby satisfying Requirement R2.3. Potential numerical instabilities are checked, and exceptions are raised if any, as per Requirement R2.8. Cycle slip flags from the receiver, if any, are checked too, as per Requirement R2.9.

IV.2. Measurement Screening and Rejection

Measurement outliers are identified by comparing prefit residuals with κ multiples of the trace of the innovation variance Equation 11, where κ is a configurable parameter *e.g.* $\kappa = 5$, and \mathbb{I} is simply an indicator function,

$$\mathbb{I} (\| \vec{v} \|_2^2 > \kappa \cdot \text{tr}(\mathbf{V})) = \begin{cases} \text{Accept if } True, \\ \text{Discard if } False, \end{cases} \quad (36)$$

The innovation covariance from 11 provides an adaptive threshold that accurately reflects the immediate prefit uncertainty, as it sums contributions from both modeled measurement noise plus current state uncertainties projected onto the measurement subspace. Adaptive thresholds more accurately reflects the underlying uncertainty of prefit residuals, and contrasts with fixed gated thresholds that must be manually tuned based on domain knowledge [20, 21]. However, careful initialization of the *a priori* state covariance and accurate measurement uncertainty modeling are needed. Overconfident initialization may cause rejection of valid measurements as $\kappa \cdot \text{tr}(\mathbf{V})$ provides overly tight bounds, while underconfident initialization may admit outliers.

IV.3. Memoryless Estimation and Monitoring of Prefit Residual Statistics

While the innovation covariance provides a snapshot estimate of prefit residual uncertainty, a moving-window estimator could capture time-varying statistics. A memoryless and statistical approach to fault detection is given in Algorithm 1,

Algorithm 1 Memoryless Estimation and Monitoring of Prefit Residual Statistics

```

1: for each computed prefit residual  $r$  do
2:    $\mu_{k+1} \leftarrow (1 - \rho)\mu_k + \rho \cdot r$                                  $\triangleright$  Fading memory update of estimated mean of prefit residuals
3:    $\sigma_{k+1}^2 \leftarrow (1 - \rho)\sigma_k^2 + \rho \cdot (r - \mu_k)$                $\triangleright$  Fading memory update of estimated sigma of prefit residuals
4:    $S_{k+1} \leftarrow (1 - \rho)S_k$                                       $\triangleright$  Decay the score of the number of outliers
5:   if  $\|r - \mu_{k+1}\|^2 > \eta \cdot \sigma_k^2$  then
6:      $S_{k+1} \leftarrow S_{k+1} + 1$                                  $\triangleright$  If prefit residual  $r$  lies outside  $\eta \cdot \sigma_k^2$  bounds, increase outlier count by +1
7:   end if
8: end for
9: if  $\left(1 - \frac{S_{k+1}}{M}\right) > g(\mu_{k+1}, \sigma_{k+1}^2)$  then
10:  do emit navigation incapability flag                             $\triangleright$  Flag incapable if number of outliers violate concentration inequalities
11: end if

```

where M is the ‘moving window’ size; $\rho \equiv 1/M$ is the forget-factor; μ_k and σ_k^2 are the empirically estimated sample mean and covariance of the prefit residuals at time k ; S_k is a fading count of outliers residing beyond the tail bounds of $\eta\sigma_k^2$ at time k ; η is a hyper-parameter; and $g(\mu_i, \sigma_i^2)$ returns a concentration inequality upper bound for the outlier fraction outside the $\eta\sigma_k^2$ tails.

The core idea of [Algorithm 1](#) is to model prefit residuals as a stationary stochastic process with non-zero decay, implying a time-invariant mean and variance [53]. These are estimated empirically using a memoryless moving window. If enough anomalous measurements occur such that the estimated outlier fraction exceeds $g(\mu_i, \sigma_i^2)$, the algorithm deems the current distribution invalid and raises an incapability flag. For general distributions, g may use Chebyshev’s Inequality [53]; for unimodal ones, the Vysochanskij-Petunin inequality applies [60, 61]. Importantly, the moving window does not retain time-series history of M samples, making its memoryless design well suited for flight computers. [Figure 9](#) gives the reader a preview ahead of the results, to the FDIR flight software response to and recovery from a deliberately injected cycle slip.

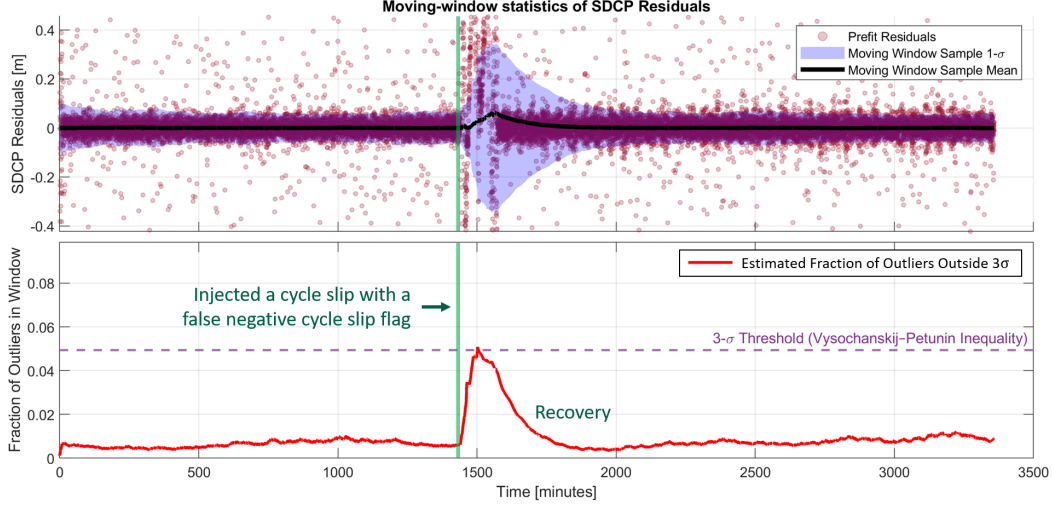


Figure 9: Plot of moving-window sample mean and variance of SDCP measurement prefit residuals (top) and moving-window estimate of number of outliers outside $\eta\sigma^2$ (bottom) for $\eta = 3$ and $M = 6000$; cycle slips were injected at $t = 24$ hours for GPS vehicles currently tracked in 6/12 active channels of one spacecraft. The software detected a fault once outlier counts violated the Vysochanskij-Petunin inequality. The filter auto-recovered after 1 orbit. Default recovery action re-initializes the mean and covariances of float ambiguities.

[Figure 9](#) shows a time-series of SDCP measurement prefit residuals, with cycle slips injected at $t = 24$ hours, from a two-spacecraft campaign initialized with a 200m along-track separation over ≈ 2.5 days. Measurements are received every 10s. Each slip was modeled as a Gaussian with bias and noise $\approx 1500 \pm 150$ cycles. Two observations followed: (1) most measurements were rejected by [Equation 36](#), and (2) accepted measurements had large enough residuals to bump up the outlier count until it exceeded g , triggering an anomaly flag. The system responded by resetting the mean and covariance of $\tilde{N}ZD$ and $\tilde{N}SD$ to their *a priori* distributions. Post-reset, the residuals and outlier fraction returned to nominal levels after 1 orbit. This exhibits successful FDIR and robust navigation by leveraging statistical guarantees in a memoryless algorithm suited for flight use.

V. NAVIGATION SOFTWARE DESIGN

V.1. Overview of Software Design and Interface

The `Navigation` class executes timely, accurate, and robust state estimation by fusing local and remote (crosslink) measurements with auxiliary data (e.g., maneuvers, attitude, ephemerides). A decision logic determines whether each incoming measurement triggers a filter update. On events e.g. state estimates, crosslink, telemetry etc, `Navigation` calls back to a `NavigationDelegate` inherited by the host class. The software emphasizes encapsulation, modularity, robustness, and efficiency. It is designed for turn-key integration into any host software (referred to here as the `Host`), without additional dependencies. The `Host` communicates via a single header interface, shown in [Figure 10](#). While written in C++17, the architecture and logic generalize to any object-oriented language. Best practices are followed to ensure development efficiency, ease of testing, and high computational performance.

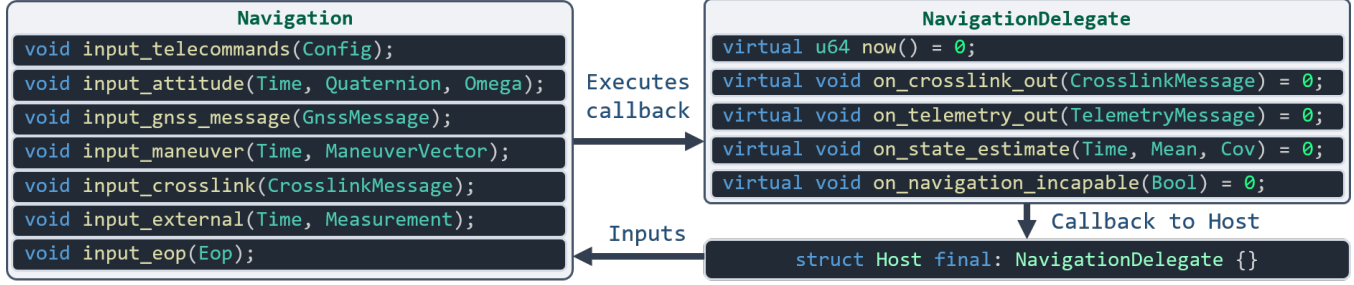


Figure 10: Software interface reflecting the implementation of Figure 2. Function signatures use C++ style syntax for illustration.

Encapsulation: Implementation details of `Navigation` are hidden behind a pointer-to-implementation design (Impl) to achieve encapsulation with separation of concerns. This reduces compile-time dependencies, as changes to `Navigation` will not require a re-compilation of the `Host` files, since the interface remains unchanged. This facilitates faster development overall.

Modularity and Flexibility of Response Logic: The callback-based interface in Figure 10 allows the `Host` to interface callbacks from `Navigation` through class inheritance, restricting method overrides solely to the host. Method overriding allows the `Host` to customize its behavior in response to callbacks, allowing for flexible response logic and ease of integration.

Robustness to Race Conditions: Ensuring data integrity of `Navigation` in real-time is critical to its successful operation. Only a single thread is ever employed in `Navigation`. The use of lock guards or mutexes is implemented to ensure that only one thread at a time may interact with `Navigation`, which protects states and data from being executed on by several concurrent operations simultaneously. This preserves state consistency, protects data from corruption, and prevents race conditions or deadlock.

Maximizing Software Efficiency with Sparsity: Sparse matrix operations are used wherever possible to reduce runtime, especially given the quadratic growth of covariance size with state dimension. A useful metric is the sparsity ratio $Sp(\mathbf{A}) = 1 - M_0/mn$ for any matrix $\mathbf{A} \in \mathbb{R}^{n \times m}$, where M_0 denotes the number of zero elements. In the time update, the process noise matrix \mathbf{Q}_t is highly sparse, as empirical accelerations do not affect clock offsets or ambiguity states. During the measurement update, the Jacobians $\mathbf{H}_t^{(x)} = \partial h / \partial \vec{x} \in \mathbb{R}^{m \times n}$ and $\mathbf{H}_t^{(w)} = \partial h / \partial \vec{w} \in \mathbb{R}^{m \times \ell}$ are also sparse, as measurements depend only on a subset of state variables. Dynamic programming techniques are adopted also for reuse of intermediate results in repeated matrix operations, reducing redundant computations and improving memory efficiency.

V.2. Data Streaming and Sequencing

A challenge observed during software integration is that data updates from sensor and actuator streams into `Navigation` are not guaranteed to arrive with a time-of-arrival that is in the same sequence as their time-stamps. This is because data are generated by several independent hardware sources per spacecraft (see Figure 11), each operating with distinct clocks and communicating over separate signal pathways. Since the recursive navigation filter progresses only forward in time, the `Navigation` interface employs a specialized `Queue` object to manage these incoming disordered data streams. The `Queue` buffers, reorders, and emits the updates in chronological order of time stamps for processing by the filter.

The `Queue` is essentially an object executing a streaming-sorting algorithm subjected to temporal constraints. Unlike batch sorting algorithms, it cannot reorder updates that have already been emitted to the filter, nor can it preemptively sort updates not yet received. This limitation means that if no assumptions are made about the maximum delay of an update entering the queue, it is impossible to perform a perfect streaming sort. For example, if the filter's current time is $t = 0$ and a GNSS measurement update with a time stamp of $t = 2$ arrives, a perfect queue would face a dilemma: it cannot emit the $t = 2$ time-stamped update immediately, as there remains the possibility of receiving an earlier $t = 1$ time-stamped update later due to latency, which would need to be emitted first. This uncertainty underscores the need for a pragmatic balance in queuing strategy.

A set of critical parameters in the design of the `Queue` are its buffer periods, or the duration for which updates are held before being forwarded to the filter. Short buffer periods enable faster integration of new information, ensuring the filter's estimate remains timely. Conversely, longer buffer periods allow the system to accommodate out-of-order messages streaming in later, reducing the likelihood of discarding updates. In the extreme case, a zero-second buffer period would immediately emit any updates as they arrive, and any incoming out-of-order updates will be dropped. The `Queue` makes the following assumptions:

1. Packets from the same hardware source will arrive in order with respect to each other.
2. Packets from any source on the local spacecraft arrive at most 2 seconds late.
3. Packets from any source on the remote spacecraft arrive at most 4 seconds late.

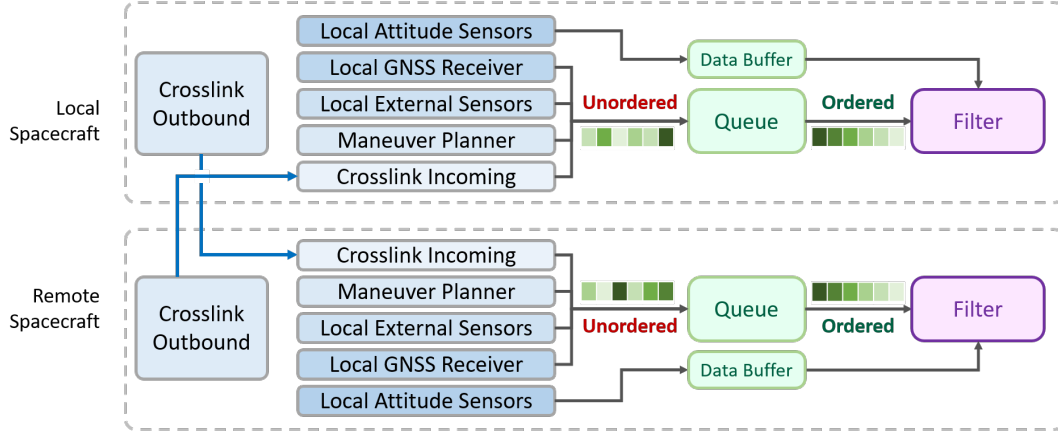


Figure 11: Queue implemented as a streaming-sorting intermediary between the Interface and the Navigation Filter.

With these assumptions, an ‘optimal’ Queue can be designed, with the understanding that any received updates that violates these assumptions will be dropped. The caveat is that Navigation then requires the ability to schedule (via a callback) any state updates in the future, past the expiration of the buffer period, if data is presently unavailable due to latency.

The Queue also intentionally facilitates seamless transitions between absolute and relative state estimation, ensuring robust operation during crosslink outages. If remote updates are unavailable beyond the 4-second buffer, the Queue continues filtering with local data alone and automatically resumes relative navigation once crosslink is restored. This transition mechanism, verified in Section VI to meet Requirement R2.6, reduces software response risks post-commissioning.

V.3. Dynamic State Resizing

Onboard compute efficiency is essential for timely, accurate state estimates that support guidance, control, and decision-making downstream. Beyond exploiting sparsity, this work introduces dynamic state resizing to reduce computational load, especially since matrix multiplications scale as $\mathcal{O}(n^3)$. Resizing is possible as not all channels remain active. After IAR, fixed integers can be treated as known constants with zero variance. Dynamic resizing removes such inactive states, reducing the state mean and covariance to only active states with non-zero variance. Floats are flushed first, integers last, as shown in Figure 12,

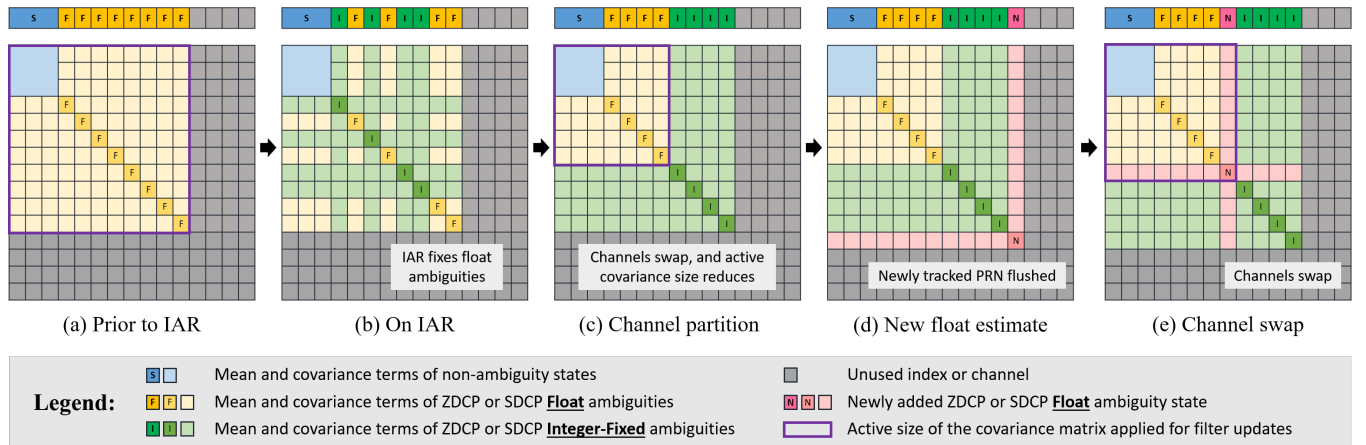


Figure 12: Dynamic resizing and channel flushing of the active covariance matrix.

In Figure 12, (a) exemplifies the state mean and covariance prior to IAR in which channels may be ZDCP or SDCP float ambiguities and the channels; (b) shows the states after successful IAR, which could be performed on any arbitrary channel index; (c) applies the channel flushing of Algorithm 2 so that integer-fixed channels are contiguously flushed with unused channels; (d) illustrates the next time instance where a previously untracked float ambiguity from a carrier phase measurement enters the state and occupies the first unused channel in the state vector; (e) performs a channel swap to flush the new float ambiguities channels with existing ones, in order to ensure that the active states remain contiguous.

Channel flushing in Algorithm 2 is key to efficient covariance resizing. It assumes zero-indexing. Let N_{float} be a tracked number of channels which remain as unresolved float ambiguities (either ZDCP or SDCP), and let `channel` be an array of channels informing whether a channel of some index i is fixed or floating. The `SwapChannel` function of Line 14 in Algorithm 2 takes as inputs the channel numbers i and j to be swapped. It swaps the matching i -th and j -th indices that match the i and j channel numbers, of the state mean \bar{x} , and then swaps both the matching i -th and j -th rows, and then the i -th and j -th columns of the state covariance Σ . This can be represented using the permutation Π as in $\bar{x} \leftarrow \Pi\bar{x}$ and $\Sigma \leftarrow \Pi\Sigma\Pi^T$. After each execution of IAR, Algorithm 2 will ensure fixed and float channels are flushed contiguously for ease of state resizing.

Algorithm 2 Channel flushing after IAR

```

1:  $i \leftarrow 0$ 
2: while  $i < N_{floats}$  do
3:   while channel[ $i$ ] is not integer fixed do
4:      $i \leftarrow i + 1$ 
5:   if  $i \geq N_{floats}$  then return
6:   end if
7: end while
8: while channel[ $N_{floats} - 1$ ] is integer fixed do
9:    $N_{floats} \leftarrow N_{floats} - 1$ 
10:  if  $i \geq N_{floats}$  then return
11:  end if
12: end while
13:  $N_{floats} \leftarrow i + 1$ 
14: SwapChannel( $i, N_{floats}$ )
15:  $i \leftarrow i + 1$ 
16: end while

```

VI. TEST CAMPAIGNS AND RESULTS

VI.1. Testbed Architecture and Modeling Assumptions

This section describes the end-to-end testbed, referenced to Figure 13, for evaluating the navigation flight software, as well as modeling assumptions in the dynamics, measurements, and simulation environment. The flow of events is scheduled in real-time via a hybrid discrete-time continuous-time event loop [62]. Uncertainty modeling with regards to ground truth dynamics, measurement generation, and spacecraft-specific contributions are summarized in Table 8, Table 9, and Table 10 respectively.

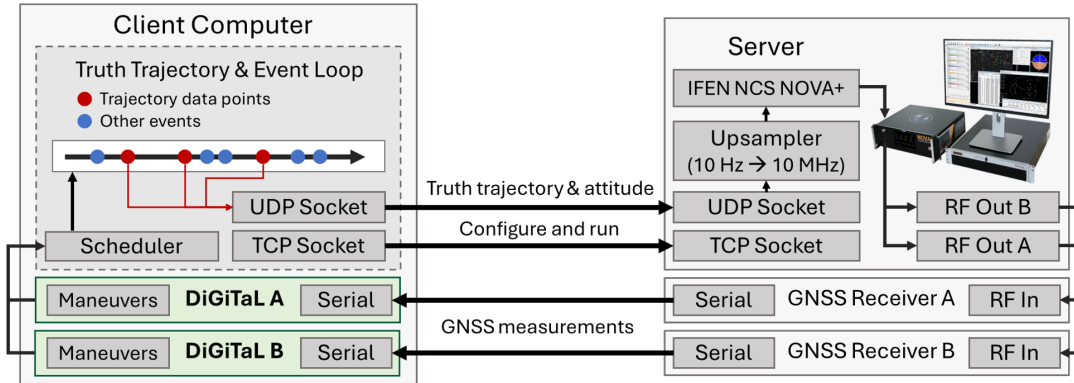


Figure 13: Hardware-in-the-loop (HIL) testbed for closed-loop evaluation of the DiGiTaL v2 software. The client executes a dynamics-driven event loop in real-time [62], transmitting truth trajectory and attitude at 10-Hz interpolation to a IFEN NCS NOVA+ GNSS signal simulator (server). GNSS RF signals then stimulate two Novatel OEM628 GNSS receivers, whose measurements are streamed via serial to two DiGiTaL software instances. Crosslink between each DiGiTaL object is software-simulated with latencies.

Table 8: Dynamics modeling

	Ground truth dynamics	Filter dynamics
State representation	Quasi-nonsingular orbital elements	Cartesian
State equations	Gauss' variational equations	Fundamental orbital differential equations
Integrator	RK45 (Dormand-Prince)	RK4 (non-adaptive step size)
Geopotential	GGM05S (60x60)	GGM05S (20x20)
Drag model	NRLMSISE 00, F10.7 = 184.6, Ap = 18.4	Harris-Priester
Solar radiation pressure	Analytical sun ephemeris with cylindrical shadow	—
Third body gravity	Analytical Sun & Moon ephemeris	—

Table 9: GNSS signal-in-space conditions modeling

GNSS signals	GPS L1 only, Block IIR-M
GNSS aperture	170 degrees
GNSS gain/phase pattern	Spherical only
GNSS ephemeris source	Broadcast (no corrections)
Ionospheric model	Klobuchar (delay only)
Receiver Earth horizon mask	-20 degrees from horizon
Receiver aperture mask	190 degrees
Receiver simulated LNA	33 dBW
Receiver gain/phase pattern	ANTCOM 1.9G1215A

Table 10: Spacecraft uncertainty parameters.

Parameter	Unit	Dist.	Value
Spacecraft mass	kg	Gaussian	0.04
Spacecraft COM	mm	Uniform	3
GNSS antenna PCO bias	mm	-	50
GNSS antenna PCO noise	mm	Gaussian	1
GNSS antenna direction	arcsec	Gaussian	30
Attitude knowledge	arcsec	Gaussian	20
Maneuver magnitude	%	Gaussian	5
Maneuver direction	arcsec	Gaussian	60

Table 11: Klobuchar ionospheric model parameters

α_1	α_2	α_3	α_4	β_1	β_2	β_3	β_4
2.794e-8	-7.451e-9	-1.192e-7	1.788e-7	137200	-98300	65540	-393200

VI.2. Requirements Verification and Compliance Tests

This section outlines compliance test scenarios in [Table 12](#), with graduating fidelity. It provides traceability by mapping surveyed requirements of [Table 4](#) to compliance tests, via the RVM in [Table 13](#). Wide test coverage stresses weak points in the software, revealing where software or navigation logic may fail. This uncovers hidden vulnerabilities, across modes of [Figure 1](#), and ensures the system can handle realistic off-nominal conditions. Test campaigns are drawn from the VISORS mission [10], due to the generalizability of the VISORS con-ops for DSS missions.

Table 12: Full set of compliance test campaigns. For brevity, only scenarios **T.4.1** and **T.7.2** are presented in detail in this paper.

Test Campaign	Test Scenarios
T.1 - Unit Tests	T.1.1 - Software built-in-tests to verify numerical correctness and function behaviour
T.2 - Initialization and Interfacing	T.2.1 - Receiver cold start test (no prior almanac)
	T.2.2 - Receiver warm start test (with prior almanac)
	T.2.3 - Sample packet test for crosslink, attitude, telecommands and propulsion
T.3 - Software Emulated GNSS in the Loop Nominal Scenarios	T.3.1 - Standby, no station-keeping, 1 day
	T.3.2 - Full campaign (standby-transfer-operations), 36 orbits
	T.3.3 - Full mission, 10 campaigns with 1 week of Standby between with role switches
T.4 - Software Emulated GNSS in the Loop for Degraded Scenarios	T.4.1 - Test Full Crosslink Outage for a Single Orbit
	T.4.2 - Full campaign, 36 orbits. Crosslink drop-rate of 1%, with 99% persistence
	T.4.3 - Full campaign, 36 orbits. GNSS drop-rate of 1%, with 75% persistence
	T.4.4 - Full campaign, 36 orbits. Maneuver packet drop-rate of 100% (no propulsion telemetry)
	T.4.5 - Full campaign, 36 orbits. Elevated noise in measurements, dynamics, and maneuvers
	T.4.6 - Full campaign, 36 orbits. Float ambiguity resolution only, forced no IAR
T.5 - Software Emulated GNSS in the Loop for Contingency Scenarios	T.5.1 - Science/operations mode, but force-interrupted with triggered escape
	T.5.2 - Science/operations mode, but force-interrupted with bus safe mode
T.6 - Software Emulated Sweep Tests	T.6.1 - Full campaign, 36 orbits, with a variable sweep over uncertainty parameters
T.7 - Hardware Emulated Real-Time GNSS in the Loop Nominal Scenarios	T.7.1 - Standby, no station-keeping, sun-pointing attitude, 1 day
	T.7.2 - Full campaign, 36 orbits, in real-time (standby-transfer-operations), with role-switch
T.8 - Hardware Earth-Fixed Live-Sky Antenna Test	T.8.1 - Live-sky daytime navigation test
	T.8.2 - Live-sky night time navigation test

Table 13: Requirements Verification Matrix (RVM) mapping compliance test in Table 12 items to navigation requirements in Table 4

	R1.1	R1.2	R1.3	R1.4	R1.5	R1.6	R2.1	R2.2	R2.3	R2.4	R2.5	R2.6	R2.7	R2.8	R2.9	R3.1	R3.2	R3.3	R3.4	R3.5	R3.6	R3.7	R3.8
T.1.1																							
T.2.1																							
T.2.2																							
T.2.3																							
T.3.1																							
T.3.2																							
T.3.3																							
T.4.1																							
T.4.2																							
T.4.3																							
T.4.4																							
T.4.5																							
T.4.6																							
T.5.1																							
T.5.2																							
T.6.1																							
T.7.1																							
T.7.2																							
T.8.1																							
T.8.2																							

All test scenarios in Table 12 are periodically run throughout development. The DiGiTaL v2 flight software was most recently reviewed, as part of a wider VISORS Flight Software review held in Stanford University, in November 2024. It was paneled by notable reviewers in the space flight community from across multiple universities, aerospace companies, and public science agencies. A brief elaboration of each test campaign is described below. For brevity, detailed results are presented from only two test scenarios **T.4.1** and **T.6.2** that represent the widest test coverage, including contingencies, out of the twenty scenarios total.

T.1: Unit tests form the foundation of software validation, with test coverage on navigation functions, state transformations, dynamics and measurement modeling, time scale conversions, coordinate rotations etc. A Continuous-Integration and Continuous-Delivery (CI/CD) pipeline integrates these tests after every software commit to ensure functional correctness and catch edge cases or unreachable states in the event of an introduced software bug, prior to any integrated tests.

T.2: Interface testing validates the accuracy and resilience of the flight software’s interaction with data sources. These tests begin with software-emulated GPS receiver packets, crosslink packets, and telecommands. Fidelity progresses to hardware-emulated packets from a NovAtel OEM628 driven by the IFEN NOVA+ GNSS signal simulator as in Figure 13, and then actual live-sky GNSS packets via rooftop antennas for a zero-baseline test. Live-sky tests validate interfacing with both cold (no prior almanac) and warm starts (with almanac) on the receiver. All interfacing algorithms are tested to ensure correct packet parsing, checksum validation, and reliable operation across all conditions.

T.3 - T.6: Software-in-the-loop GNSS emulation is a critical enabler for rapid development and deployment, due to faster-than-real-time testing. Modeling realism remains consistent with Tables 8, 9, 10 and 11. Furthermore, it permits testing **Navigation** with other emulated subsystems (e.g., Guidance, Control, Safety) for full mission simulation of VISORS [10]. This framework allows thorough performance evaluation across performance degraded scenarios (**T.4**), contingency scenarios such as safe modes or during an escape trajectory (**T.5**), and robustness to variations in uncertainty parameters via sweep tests (**T.6**). These campaigns graduates the software readiness ahead of an integrated hardware-in-the-loop testing.

T.7 - T.8: Hardware-in-the-loop (HIL) GNSS testing represents the culmination of the test campaign, validating the full analog-digital signal chain with the DiGiTaL v2 navigation flight software at its core. It exercises all components of the software: interfacing, functionality, and performance, in real-time with latencies, and with other software subsystems e.g. Guidance, Controller, and Safety, in closed-loop. GNSS measurements generated by the hardware in Figure 13 rely on ground truth states, which are driven by the event loop [62]. The event loop coordinates the dynamics and the timing asynchronously into a single thread across all threads on each hardware unit (the IFEN NOVA+, the local host running the event loop, and each instance of the **Navigation** software. This achieves mission-representative validation of DiGiTaL v2’s navigation performance under realistic and real-time operational conditions.

VL3. Compliance Test Results: VISORS Full Campaign, Hardware-in-the-Loop in Real-Time

This section details a full VISORS campaign scenario **T.7.2** with GNSS hardware-in-the-loop as per Figure 13 in real-time. VISORS is a distributed telescope mission for high-resolution imaging of the Sun in the extreme ultraviolet spectrum, using two 6U CubeSats flying in formation in a Sun-synchronous low-Earth orbit. An Optics Spacecraft (OSC) carries a photon sieve lens, while signals passing through the lens is focused on a Detector Spacecraft (DSC). Observations happen at a 40m baseline with sub-cm alignment requirements. Elaborated details of the concept of operations, as well as specifics on the other subsystems can be found in references [9, 10]. Relative orbit configurations are in Table 14,

Table 14: Reference orbit and quasi-nonsingular relative orbital elements per mode for test conditions. Epoch is 12 AM, 1 Oct 2024 GPST.

Reference orbit		Relative orbit modes		
Element	Sun Sync Parameters	Element	Standby (m)	Science (m)
a (km)	$R_E + 500$	$a\delta a$	0	-2.62
e (-)	0.004	$a\delta\lambda$	0	45.21
i (deg)	97.8	$a\delta e_x$	0	-34.51
Ω (deg)	157.5	$a\delta e_y$	200	4.78
$u(t_0)$ (deg)	0	$a\delta i_x$	0	-18.72
LTAN	10:00AM	$a\delta i_y$	200	2.72

T.7.2 conducts a full test campaign that initializes the DSC and OSC in Standby, transitions to Transfer, and then to Science mode, performing one observation per Science orbit. A Laser Rangefinder (LRF) on the OSC and a Reflector on the DSC enable alignment verification via range measurements. Up to 10 Science orbits, and thus 10 alignment attempts, are executed. Midway, a role-switch maneuver transfers relative orbit control between spacecraft to validate that both `Navigation` instances remain uninterrupted and performant. Relative navigation results are shown in Figure 14.

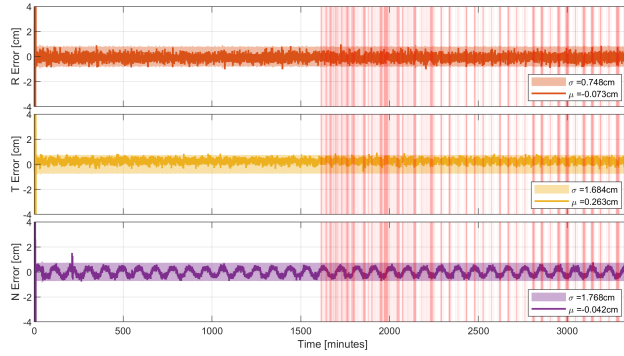
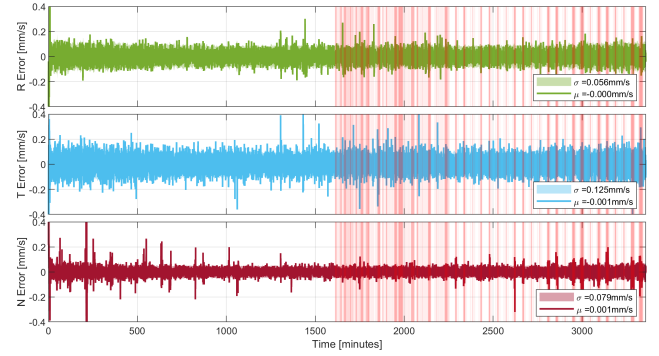
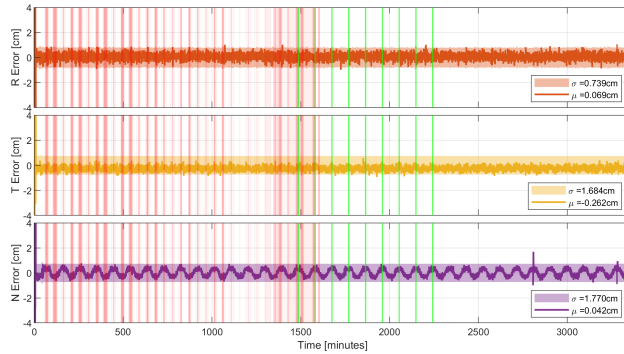
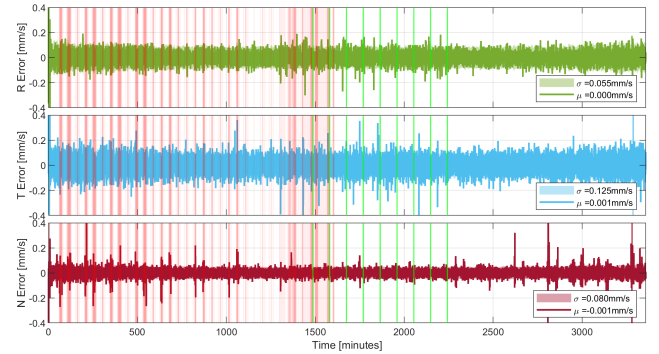
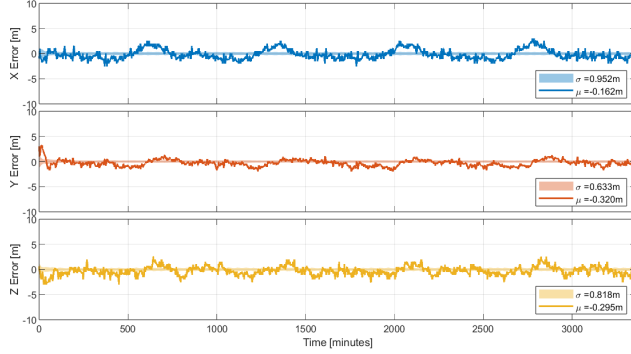
**14a:** Relative position error and covariance estimated by DSC**14b:** Relative velocity error and covariance estimated by DSC**14c:** Relative position error and covariance estimated by OSC**14d:** Relative velocity error and covariance estimated by OSC

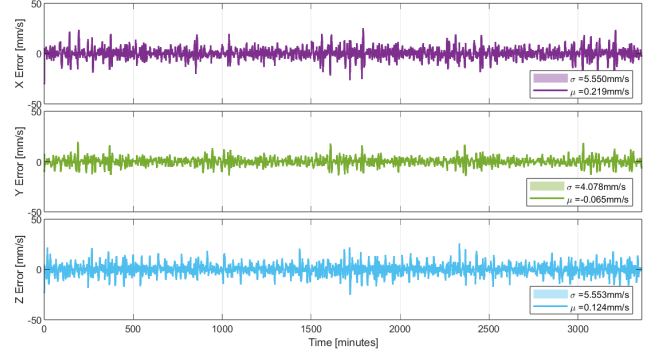
Figure 14: Relative trajectory errors and covariance throughout the campaign. Translucent red lines are indicative of maneuvers, each with a maximum impulse bit of 2mm/s; while green lines are indicative of reception of LRF measurements for alignment confirmation. Maneuver control was handed over to the other spacecraft mid-way, so as to test the software’s capability to handle role switches. All 10 alignment attempts recorded LRF readings, out of which 4 led to successful observation attempts.

Integers were batch-resolved by $t = 8$ minutes. For the remainder of the campaign, nearly all float ambiguities become integer-resolved within one measurement update due to the high confidence of the filter post-IAR. The filter’s *a priori* COM-to-PCO consider covariance assumes 5mm uncertainty per axis, with true body-frame errors detailed in Table 10. Despite a 5cm PCO bias—an order of magnitude larger and unknown to the filter—Figure 14a and Figure 14c show the filter’s covariance envelope converging conservatively around the true error, indicating robust state estimation. One possible explanation for this desirable phenomenon is due to the state vector’s flexibility: spacecraft clock offsets and 24 ZDCP ambiguity channels offer

sufficient degrees of freedom to absorb static measurement biases. Remnant time-varying bias components (from PCVs or attitude-induced COM-to-PCO lever arm changes) manifest in prefit residuals, shaping the steady-state covariance, with the influence of the consider parameters included. Next, absolute position and velocity estimation in the ECI frame is shown in Figure 15; estimated empirical accelerations in Figure 16a; estimated receiver clock offsets in Figure 16b; a visual of the relative trajectory with the LRF scatter grouping in Figure 17; and residuals for GRAPHIC and SDCP are shown in Figure 18,

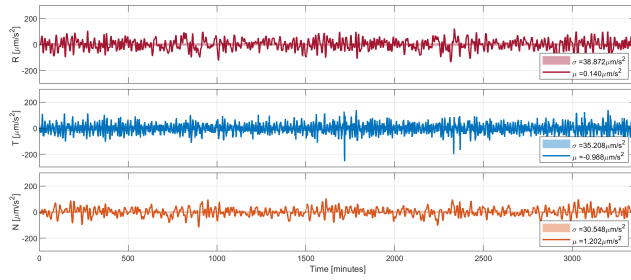


15a: Absolute ECI position errors of the DSC

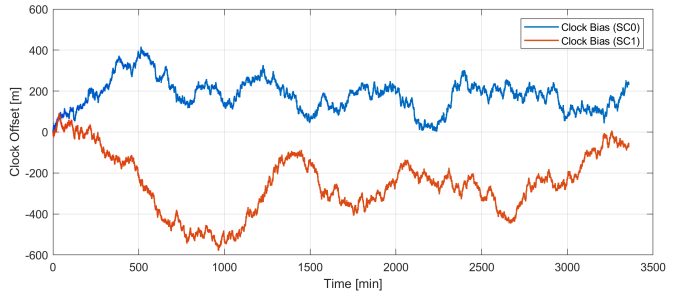


15b: Absolute ECI velocity errors of the DSC

Figure 15: Absolute ECI state errors of the DSC. OSC results are similar and omitted for brevity.

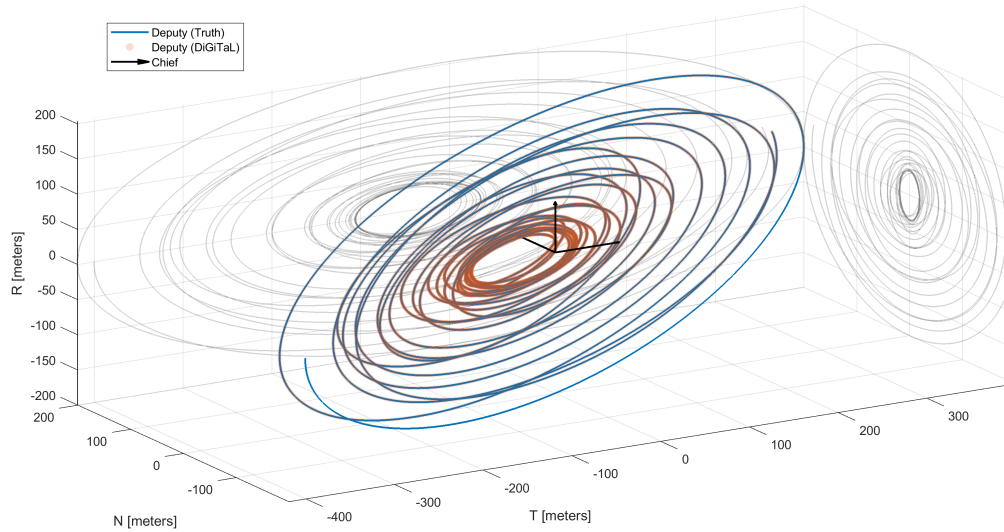


16a: Empirical accelerations of the DSC. OSC results are similar.

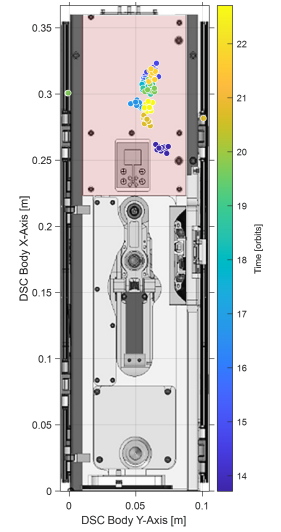


16b: Estimated receiver clock offsets [m] for both spacecraft.

Figure 16: Empirical accelerations and receiver clock offsets.

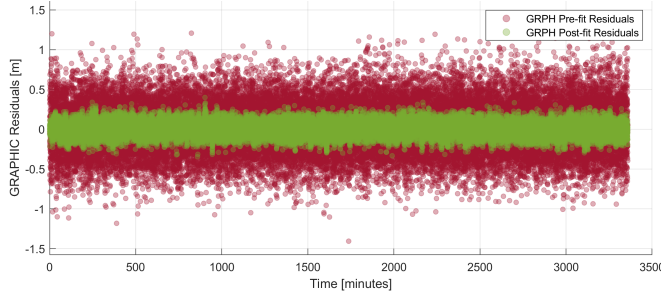


17a: Plot of true and estimated relative orbit, with DSC at the origin.

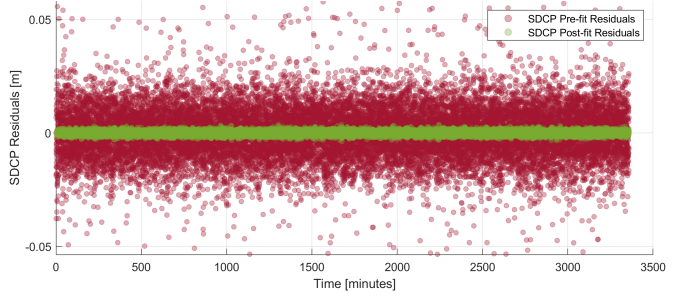


17b: LRF scatter grouping

Figure 17: Visualization of the true and estimated relative trajectory, with an overlay of the received LRF scatter plots on the DSC reflector panel in the body frame. LRF scatter groupings fall within an ellipsoid of 3.5×2.5 cm measured by the semi-axes.



18a: GRAPHIC (local) residuals for the DSC

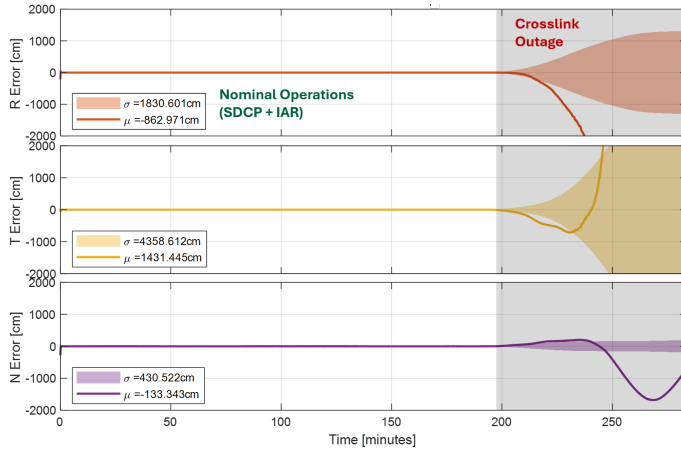


18b: SDCP residuals for the DSC

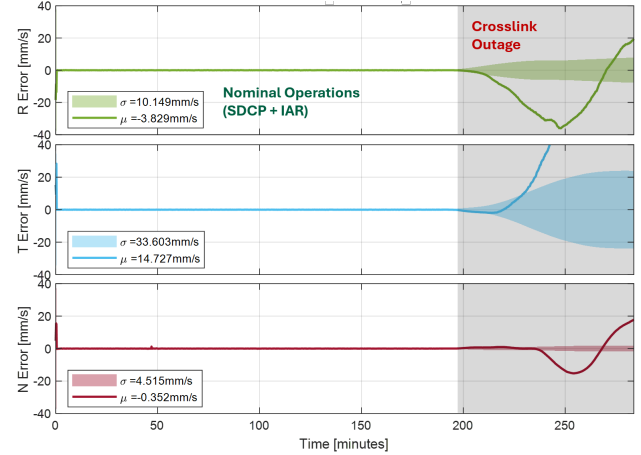
Figure 18: Pre- and post-fit residuals for GRAPHIC and SDCP in the DSC. OSC results are similar and hence omitted for brevity.

VI.4. Compliance Test Results: VISORS Standby, with Simulated Crosslink Outage

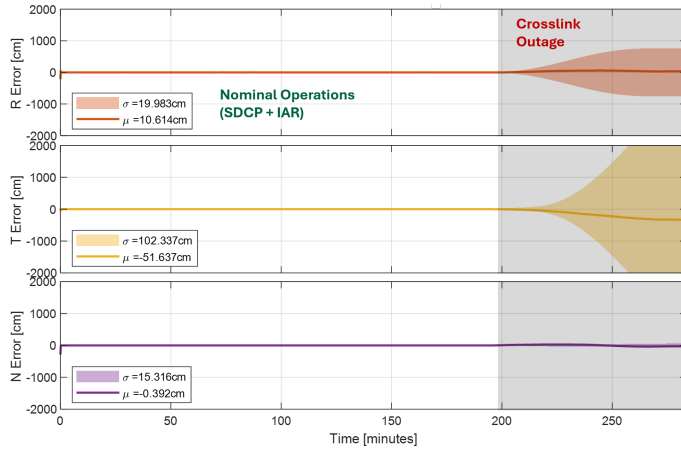
Scenario T.4.1 evaluates the impact of process noise modeling on orbit prediction accuracy during crosslink outages. A performance comparison is conducted between the legacy diagonal-only process noise model which uses manually tuned diagonal parameters from DiGiTaL v1, and the proposed new analytical process noise in DiGiTaL v2 that captures inter-state correlations. Both configurations begin with nominal navigation for 2 orbits, followed by a crosslink outage requiring open-loop orbit propagation due to missing remote measurements.



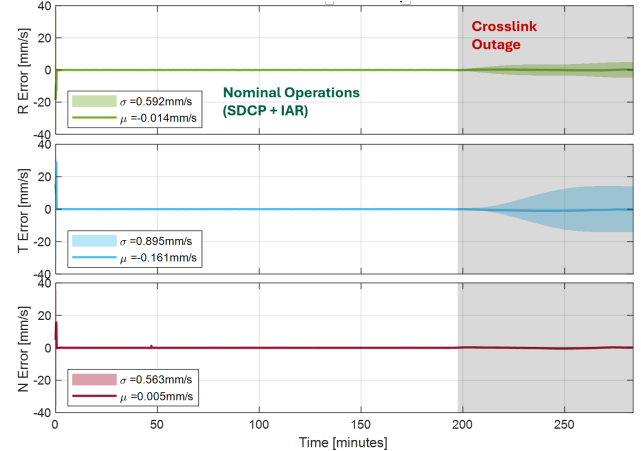
19a: Relative position error during outage, diagonal-only process noise



19b: Relative velocity error during outage, diagonal-only process noise



19c: Relative position error during outage, correlated process noise (30)



19d: Relative velocity error during outage, correlated process noise (30)

Figure 19: Plots of relative navigation performance (position and velocity in RTN) using the legacy manually tuned diagonal-only process noise in DiGiTaL v1 (*top*), versus the proposed correlated analytical process noise model of DiGiTaL v2 (*bottom*).

As shown in Figure 19, the new correlated process noise model significantly improves relative position and velocity errors during the outage. These results demonstrate that a process noise model that is physically consistent with empirical accelerations significantly improves prediction fidelity under degraded navigation. It also indicates that the software logic satisfies the requirement for seamless transition between relative and absolute-only navigation modes, as the crosslink goes non-operational.

VI.5. Comparative Performance and Runtime Analyses with Predecessor Software

A comparative analyses of performance (Table 15) and runtime (Table 16) was conducted between DiGiTaL v2 and its predecessor [21], using Test Campaign T.3.2 and T.4.1. To ensure a fair ceteris paribus comparison between two versions of the software, *all* modeling parameters (dynamics, measurements, simulation environment) applied are identical to both. The same Mersenne Twister seeds are also applied in the simulation environment to ensure identical pseudorandom inputs that stimulate the flight software. The computer-under-test, which runs the flight software, is a **Xilinx Zynq-7000 System-on-Chip**, an exact representation of the VISORS flight computer. It is a two-core embedded processor, ARM Cortex-A9, 650 MHz, where the operating system is PetaLinux 2016.2, running on Linux Kernel v4.4.

Table 15: Root-mean-square errors (RMSE) computed, with VISORS observation success rates, using legacy and improved filter designs. Outage scenario follows Scenario T.4.1, with RMSE computed during the outage period of 1 orbit

	Filter Type	Abs. Pos. RMSE [meters]	Abs. Vel. RMSE [mm/s]	Rel. Pos. RMSE [mm]	Rel. Vel. RMSE [mm/s]	Rel. Pos. (outage) RMSE [meters]	Rel. Vel. (outage) RMSE [mm/s]	VISORS Observation Success
DiGiTaL v1	EKF	12.409	15.561	1.828	0.041	55.838	45.802	1 / 10
	EKF-UKF Hybrid	10.388	13.551	1.820	0.041	53.436	44.745	1 / 10
DiGiTaL v2	Regularized CEKF (Joseph Form)	0.695	4.379	1.790	0.040	1.054	1.204	2 / 10
	Sparse Regularized CEKF (Non-Joseph-Form)	0.687	4.351	1.813	0.041	1.196	1.289	2 / 10

Table 16: Analyses of averaged runtimes, units in [ms] for core navigation function calls on the VISORS computers (Xilinx Zynq-7000 SoC). IAR runtime is recorded as the time of largest batch size to fix, rather than average, since IAR runtime scales with the ambiguity vector size.

	Filter Type [ms]	Time Update [ms]	GRAPHIC [ms]	SDCP [ms]	IAR (max) [ms]	Total [ms]
DiGiTaL v1	EKF	1.384	14.284	14.697	0.861	31.226
	EKF-UKF Hybrid	1.386	20.806	34.226	0.863	57.281
DiGiTaL v2	Regularized CEKF (Joseph Form)	1.414	19.208	19.726	0.908	41.256
	Sparse Regularized CEKF (Non-Joseph-Form)	1.405	1.043	1.515	0.884	4.847

In terms of accuracy, the filter designs of DiGiTaL v2 exceed its predecessor in all areas in both nominal and off-nominal (outage) conditions. Significant improvements were observed in open-loop orbit prediction accuracy and absolute position estimation, by virtue of the improved process noise modeling. Marginal improvements were observed in relative state accuracy, which is expected as accuracies are approaching the thermal noise limits of SDGP measurements post-IAR. Performance RMSE is computed across $\approx 19,500$ measurements each for GRAPHIC and SDGP in the 36-orbit full campaign, and about $\approx 1,625$ measurements in the 1-orbit crosslink outage scenario.

In terms of runtime, as elaborated prior, a trade-off exists where the Sparse-Regularized CEKF in non-Joseph form is significantly faster and more memory-efficient but does not provide a mathematical guarantee on a positive definite state covariance. In contrast, the Joseph form does do so, but at the cost of significantly slower execution speed, comparable to its predecessor, because matrix terms in Joseph form are dense. This choice depends on the balance between efficiency and robustness. Hence, the software has enabled a feature to toggle on or off the positive-definiteness feature of the CEKF, by means of telecommands. Regardless of either settings for the CEKF, the navigation runtime still meet the timing requirements of the VISORS mission for navigation state update intervals.

VII. CONCLUSION

This paper presents a complete CDGNSS-based navigation flight software package tailored for high-precision DSS missions. A rigorous, requirements-driven design process led to DiGiTaL v2, an end-to-end architecture emphasizing numerical stability, computational efficiency, and fault detection with isolation and recovery. The modular software framework and optimization strategies facilitate integration into emerging DSS host systems. Performance is validated through a multi-stage test campaign culminating in flight-like results from the VISORS mission. A carefully designed test campaign, with graduated fidelity, enables rapid failure point traceability via bisection. Comprehensive documentation of the design, development, and outcomes of this work aims to position the DiGiTaL v2 as a reference for emerging missions with stringent relative navigation needs. Viable research directions to improve the software in terms of scalability, robustness, and fault tolerance have been identified.

Acknowledgements: The authors gratefully acknowledge the support of the the NSF (Award No. 1936663), as well as DSO National Laboratories for fellowship support. The authors also extend their gratitude towards members of the VISORS team at large, including our cross-institution collaborators.

REFERENCES

- [1] Simone D'Amico. *Autonomous Formation Flying in Low Earth Orbit*. PhD thesis, TU Delft, 2010.
- [2] PJG Teunissen. A new method for fast carrier phase ambiguity estimation. In *Proceedings of 1994 IEEE Position, Location and Navigation Symposium-PLANS'94*, pages 562–573. IEEE, 1994.
- [3] Remco Kroes, Oliver Montenbruck, William Bertiger, and Pieter Visser. Precise grace baseline determination using gps. *GPS Solutions*, 9:21–31, 2005.
- [4] Oliver Montenbruck, Simone D'Amico, Jean-Sebastien Ardaens, and Martin Wermuth. Carrier phase differential gps for leo formation flying—the prisma and tandem-x flight experience. *Paper AAS*, pages 11–489, 2011.
- [5] Simone D'Amico and Oliver Montenbruck. Differential gps: An enabling technology for formation flying satellites. In *Small Satellite Missions for Earth Observation: New Developments and Trends*, pages 457–465. Springer, 2010.
- [6] Simone D'Amico, Jean-Sebastien Ardaens, and Sergio De Florio. Autonomous formation flying based on gps - prisma flight results. *Acta Astronautica*, 82(1):69–79, 2013. ISSN 0094-5765. doi: <https://doi.org/10.1016/j.actaastro.2012.04.033>. 6th International Workshop on Satellite Constellation and Formation Flying.
- [7] Niels H. Roth. *Navigation and Control Design for the CanX-4/-5 Satellite Formation Flying Mission*. PhD thesis, University of Toronto, 2010.
- [8] Erin Kahr, Niels Roth, Oliver Montenbruck, Ben Risi, and Robert E. Zee. Gps relative navigation for the canx-4 and canx-5 formation-flying nanosatellites. *Journal of Spacecraft and Rockets*, 55(6):1545–1558, 2018. doi: 10.2514/1.A34117.
- [9] Adam Koenig, Simone D'Amico, and E Glenn Lightsey. *Formation Flying Orbit and Control Concept for the VISORS Mission*, chapter 0, page 0. AIAA, 2021. doi: 10.2514/6.2021-0423.
- [10] Tommaso Guffanti, Toby Bell, Samuel Y. W. Low, Mason Murray-Cooper, and Simone D'Amico. Autonomous guidance, navigation and control of the visors formation flying mission. In *AAS/AIAA Astrodynamics Specialist Conference*, page 0, Big Sky, Montana, 2023.
- [11] Vincent Giraldo and Simone D'Amico. Precise real-time relative orbit determination for large-baseline formations using gnss. In *Proceedings of the 2021 International Technical Meeting of The Institute of Navigation*, pages 366–384, 2021.
- [12] Adam W Koenig, Simone D'Amico, Bruce Macintosh, and Charles J Titus. Formation design analysis for a miniaturized distributed occulter/telescope in earth orbit. In *International Symposium on Space Flight Dynamics (ISSFD)*. DLR German Space Operations Center and the European Space Agency, 2015.
- [13] Bruce Macintosh, Simone D'Amico, Adam Koenig, Eduardo Bendek, Keith Grogran, Stuart Shalkan, A. Madurowicz, R. de Rosa, T. Greene, J. Debes, E. Douglas, R. Jensen-Clem, G. Duchene, and T. Esposito. Miniature distributed occulter telescope (mdot) publicly released project report. Technical report, Stanford University, Space Rendezvous Laboratory, 2022.
- [14] John D Monnier, Prachet Jain, Shashank Kalluri, James Cutler, Simone D'Amico, Glenn Lightsey, Leonid Pogorelyuk, Gautam Vasisht, Kerri Cahoy, and Michael Meyer. Stari: starlight acquisition and reflection toward interferometry. In *Space Telescopes and Instrumentation 2024: Optical, Infrared, and Millimeter Wave*, volume 13092, pages 1095–1107. SPIE, 2024.
- [15] Takahiro Ito, Kiwamu Izumi, Isao Kawano, Ikkoh Funaki, Shuichi Sato, Tomotada Akutsu, Kentaro Komori, Mitsuru Musha, Yuta Michimura, Satoshi Satoh, et al. Silvia: Ultra-precision formation flying demonstration for space-based interferometry. *arXiv preprint arXiv:2504.05001*, 2025.
- [16] Tobe' Corazzini, Andrew Robertson, John Carl Adams, Arash Hassibi, and Jonathan P How. Gps sensing for spacecraft formation flying. In *Proceedings of the 10th International Technical Meeting of the Satellite Division of The Institute of Navigation (ION GPS 1997)*, pages 735–744, 1997.
- [17] Gokhan Inalhan, Franz D Busse, and Jonathan P How. Precise formation flying control of multiple spacecraft using carrier-phase differential gps. In *AAS/AIAA Space Flight Mechanics Meeting, Clearwater, FL*, pages 23–26, 2000.
- [18] F Scala, C Colombo, GVM Gaia, M Martin-Neira, et al. Gnss-based navigation for a remote sensing three-satellite formation flying. In *SpaceOps 2021 Virtual Edition*, pages 1–18. 16th International Conference on Space Operations, 2021.
- [19] Hanjoon Shim, O-Jong Kim, Sunkyoung Yu, Changdon Kee, Dong-Hyun Cho, and Hae-Dong Kim. Precise in-orbit relative navigation technique for rendezvous mission of cubesats using only gps receivers. *CEAS Space Journal*, 16(1):117–137, 2024.
- [20] Vincent Paul Giraldo and Simone D'Amico. Distributed multi-gnss timing and localization for nanosatellites. *NAVIGATION*, 66(4):729–746, 2019. doi: 10.1002/navi.337.
- [21] Vincent Paul Giraldo. *Precision Navigation of Miniaturized Distributed Space Systems using GNSS*. PhD thesis, Stanford University, 2021.
- [22] Justin J Kruger, Tommaso Guffanti, Tae Ha Park, Mason Murray-Cooper, Samuel YW Low, Toby Bell, Simone D'Amico, Christopher W Roscoe, and Jason Westphal. Adaptive end-to-end architecture for autonomous spacecraft navigation and control during rendezvous and proximity operations. In *AIAA SCITECH 2024 Forum*, page 0430, 2024.
- [23] Samuel YW Low and Simone D'Amico. Precise distributed satellite navigation: Differential gps with sensor-coupling for integer ambiguity resolution. In *2024 IEEE Aerospace Conference*, pages 1–18. IEEE, 2024.
- [24] Samuel Low and Mykel Kochenderfer. Optimal pointing sequences in spacecraft formation flying using online planning with resource con-

- straints. In *Learning for Dynamics and Control Conference*, pages 355–365. PMLR, 2022.
- [25] S. D’Amico, J.-S. Ardaens, and R. Larsson. Spaceborne autonomous formation-flying experiment on the prisma mission. *Journal of Guidance, Control, and Dynamics*, 35(3):834–850, 2012. doi: 10.2514/1.55638.
- [26] Richard P. Kornfeld, Bradford W. Arnold, Michael A. Gross, Neil T. Dahya, William M. Klipstein, Peter F. Gath, and Srinivas Bettadpur. Grace-fo: The gravity recovery and climate experiment follow-on mission. *Journal of Spacecraft and Rockets*, 56(3):931–951, 2019. doi: 10.2514/1.A34326.
- [27] Yaowei Xia, Xin Liu, Jinyun Guo, Zhouming Yang, Linhu Qi, Bing Ji, and Xiaotao Chang. On gps data quality of grace-fo and grace satellites: Effects of phase center variation and satellite attitude on precise orbit determination. *Acta geodetica et geophysica*, 56:93–111, 2021.
- [28] John Bowen, Ai Tsuda, John Abel, and Marco Villa. Cubesat proximity operations demonstration (cpod) mission update. In *2015 IEEE Aerospace Conference*, pages 1–8. IEEE, 2015.
- [29] Christopher WT Roscoe, Jason J Westphal, and Ehson Mosleh. Overview and gnc design of the cubesat proximity operations demonstration (cpod) mission. *Acta Astronautica*, 153:410–421, 2018.
- [30] J Salvador Llorente, Alfredo Agenjo, Carmelo Carrascosa, Cristina de Negueruela, Agnes Mestreau-Garreau, Alexander Cropp, and Andrea Santovincenzo. Proba-3: Precise formation flying demonstration mission. *Acta Astronautica*, 82(1):38–46, 2013.
- [31] Jean-Sébastien Ardaens, Simone D’Amico, and Alexander Cropp. Gps-based relative navigation for the proba-3 formation flying mission. *Acta Astronautica*, 91:341–355, 2013.
- [32] Werner Enderle, Francesco Gini, Erik Schönmann, and Volker Mayer. Proba-3 precise orbit determination based on gnss observations. In *Proceedings of the 32nd International Technical Meeting of the Satellite Division of The Institute of Navigation (ION GNSS+ 2019)*, pages 1187–1198, 2019.
- [33] John D Monnier et al. A realistic roadmap to formation flying space interferometry. *arXiv preprint arXiv:1907.09583*, 2019.
- [34] Stephen J Kapurch. *NASA systems engineering handbook*. Diane Publishing, 2010.
- [35] Adam W. Koenig and Simone D’Amico. Robust and safe n-spacecraft swarming in perturbed near-circular orbits. *Journal of Guidance, Control, and Dynamics*, 41(8):1643–1662, 2018. doi: 10.2514/1.G003249.
- [36] Vincent Paul Giraldo, Michelle Chernick, and Simone D’Amico. Guidance, navigation, and control for the dwarf formation-flying mission. In *AAS/AIAA Astrodynamics Specialist Conference, South Lake Tahoe, CA*, page 0, 2020.
- [37] Per K Enge and Pratap Misra. *The Global Positioning System: Signals, Measurements, and Performance (Second Edition)*. Ganga-Jamuna Press, 2006.
- [38] Ken Shoemake. Animating rotation with quaternion curves. In *Proceedings of the 12th annual conference on Computer graphics and interactive techniques*, pages 245–254, 1985.
- [39] Mark L. Psiaki and Shan Mohiuddin. Modeling, analysis, and simulation of gps carrier phase for spacecraft relative navigation. *Journal of Guidance, Control, and Dynamics*, 30(6):1628–1639, 2007. doi: 10.2514/1.29534.
- [40] Kevin Gutsche, Thomas Hobiger, and Stefan Winkler. Addressing inaccurate phase center offsets in precise orbit determination for agile satellite missions. *NAVIGATION: Journal of the Institute of Navigation*, 71(4), 2024.
- [41] Shane Lowe, Maxim Markevitch, and Simone D’Amico. Relative navigation and pointing error budget for an x-ray astronomy formation-flying mission. In *Proceedings of the 44th Annual American Astronautical Society Guidance, Navigation, and Control Conference*, 2022, pages 1433–1445. Springer, 2022.
- [42] Renato Zanetti, Kyle J. DeMars, and Robert H. Bishop. Underweighting nonlinear measurements. *Journal of Guidance, Control, and Dynamics*, 33(5):1670–1675, 2010. doi: 10.2514/1.50596.
- [43] J Russell Carpenter and Christopher N D’souza. Navigation filter best practices. Technical report, NASA, 2018.
- [44] Stanley F Schmidt. Application of state-space methods to navigation problems. In *Advances in control systems*, volume 3, pages 293–340. Elsevier, 1966.
- [45] Andrew H Jazwinski. *Stochastic processes and filtering theory*. Academic Press, Inc., 1970.
- [46] Drew Woodbury and John Junkins. *On the Consider Kalman Filter*, chapter 0, page 0. AIAA, 2010. doi: 10.2514/6.2010-7752.
- [47] F. H. Schlee, C. J. Standih, and N. F. Toda. Divergence in the kalman filter. *AIAA Journal*, 5(6):1114–1120, 1967. doi: 10.2514/3.4146.
- [48] Thomas P Yunck. Coping with the atmosphere and ionosphere in precise satellite and ground positioning. *Washington DC American Geophysical Union Geophysical Monograph Series*, 73:1–16, 1993.
- [49] Rudolph Emil Kalman. A new approach to linear filtering and prediction problems. *ASME Digital Collection*, 1960.
- [50] Oliver Montenbruck and Eberhard Gill. *Satellite Orbits: Models, Methods and Applications*. Springer, 2010.
- [51] J Russell Carpenter and Kyle T Alfriend. Navigation accuracy guidelines for orbital formation flying. *The Journal of the Astronautical Sciences*, 53:207–219, 2005.
- [52] Jonathan P How, Louis S Breger, Megan Mitchell, Kyle T Alfriend, and Russell Carpenter. Differential semimajor axis estimation performance using carrier-phase differential global positioning system measurements. *Journal of guidance, control, and dynamics*, 30(2):301–313, 2007.
- [53] Robert G Gallager. *Stochastic processes: theory for applications*. Cambridge University Press, 2013.
- [54] Nathan Stacey and Simone D’Amico. Analytical process noise covariance modeling for absolute and relative orbits. *Acta Astronautica*, 194:34–47, 2022.
- [55] Nathan Stacey and Simone D’Amico. Adaptive and dynamically constrained process noise estimation for orbit determination. *IEEE Transactions on Aerospace and Electronic Systems*, 57(5):2920–2937, 2021.
- [56] X W Chang, X Yang, and T Zhou. Mlambda: A modified lambda method for integer least-squares estimation. *Journal of Geodesy*, 79:552–565, 2005.
- [57] Peter Teunissen. The invertible gps ambiguity transformations. *Manuscripta Geodetica*, 20:489–497, 1995.
- [58] PJG Teunissen. Success probability of integer gps ambiguity rounding and bootstrapping. *Journal of geodesy*, 72:606–612, 1998.
- [59] Peter JG Teunissen and Dennis Odijk. Ambiguity dilution of precision: definition, properties and application. In *Proceedings of the 10th International Technical Meeting of the Satellite Division of The Institute of Navigation (ION GPS 1997)*, pages 891–899, 1997.
- [60] DF Vysochanskij and Yu I Petunin. Justification of the 3σ rule for unimodal distributions. *Theory of Probability and Mathematical Statistics*, 21(25-36), 1980.
- [61] Friedrich Pukelsheim. The three sigma rule. *The American Statistician*, 48(2):88–91, 1994.
- [62] Toby Bell and Simone D’Amico. Event-driven simulation for rapid iterative development of distributed space flight software. In *2025 IEEE Aerospace Conference*. IEEE, 2025.